

1 **Revision #1 (MS# 6044)**

2 **An ab-initio study of the energetics and geometry of sulfide, sulfite and sulfate**  
3 **incorporation into apatite: The thermodynamic basis for using this system as an**  
4 **oxybarometer**

5 **YoungJae Kim<sup>1\*</sup>, Brian Konecke<sup>1</sup>, Adrian Fiege<sup>1-2</sup>, Adam Simon<sup>1</sup>, Udo Becker<sup>1</sup>**

6 <sup>1</sup>University of Michigan, Department of Earth and Environmental Sciences, Ann Arbor, MI  
7 48109-1005, USA

8 <sup>2</sup>American Museum of Natural History, Department of Earth and Planetary Sciences, New York,  
9 NY 10024-5192, USA

10 \* Corresponding author; E-mail: [youngjkm@umich.edu](mailto:youngjkm@umich.edu)

11 **Abstract**

12 Despite many studies reporting the presence of S-bearing apatite in igneous and  
13 hydrothermal systems, the oxidation states and incorporation mechanisms of S in the apatite  
14 structure remain poorly understood. In this study, we use ab-initio calculations to investigate the  
15 energetics and geometry of incorporation of S with its oxidation states S<sup>6+</sup>, S<sup>4+</sup>, and S<sup>2-</sup> into the  
16 apatite end-members fluor-, chlor-, and hydroxylapatite, [Ca<sub>10</sub>(PO<sub>4</sub>)<sub>6</sub>(F,Cl,OH)<sub>2</sub>]. The relative  
17 stability of different oxidation states of S in apatite is evaluated by using balanced reaction  
18 equations where the apatite host and a solid S-bearing source phase (e.g., gypsum for S<sup>6+</sup> and  
19 troilite for S<sup>2-</sup>) are the reactants, and the S-incorporated apatite and an anion sink phase are the  
20 products. Here, the reaction energy of the balanced equation indicates the stability of the  
21 modeled S-incorporated apatite relative to the host apatite, the source, and sink phases. For the  
22 incorporation of S into apatite, coupled substitutions are necessary to compensate for charge

23 imbalance. One possible coupled substitution mechanism involves the replacement of  $\text{La}^{3+} +$   
24  $\text{PO}_4^{3-} \leftrightarrow \text{Ca}^{2+} + \text{SO}_4^{2-}$ . Our results show that the incorporation of  $\text{SO}_4^{2-}$  into La- and Na-bearing  
25 apatite,  $\text{Ca}_8\text{NaLa}(\text{PO}_4)_6(\text{F},\text{Cl},\text{OH})_2$ , is energetically favored over the incorporation into La- and  
26 Si-bearing apatite,  $\text{Ca}_9\text{La}(\text{PO}_4)_5(\text{SiO}_4)(\text{F},\text{Cl},\text{OH})_2$  (the difference in incorporation energy,  $\Delta E_{rxn}$ ,  
27 is 10.7 kJ/mol). This thermodynamic gain is partially attributed to the electrostatic contribution  
28 of  $\text{Na}^+$ , and the energetic contribution of  $\text{La}^{3+}$  to the stability of  $\text{SO}_4^{2-}$  incorporated into the  
29 apatite structure. Co-incorporation of  $\text{SO}_4^{2-}$  and  $\text{SO}_3^{2-}$  is energetically favored when the lone pair  
30 electrons of  $\text{SO}_3^{2-}$  face towards the anion column site, compared to facing away from it.

31 Full or partial incorporation of  $\text{S}^{2-}$  is favored on the column anion site in the form of  
32  $[\text{Ca}_{10}(\text{PO}_4)_6\text{S}]$  and  $[\text{Ca}_{20}(\text{PO}_4)_{12}\text{SX}_2]$ , where X = F, Cl, or OH. Upon full incorporation (i.e.,  
33 replacing *all* column ions by sulfide ions),  $\text{S}^{2-}$  is positioned in the anion column at  $z = 0.5$  (half  
34 way between the mirror planes at  $z = 1/4$  and  $z = 3/4$ ) in the energy-optimized structure. The  
35 calculated energies for partial incorporation of  $\text{S}^{2-}$  demonstrate that in an energy-optimized  
36 structure,  $\text{S}^{2-}$  is displaced from the mirror plane at  $z = 1/4$  or  $3/4$ , by 1.0 to 1.6 Å, depending on  
37 the surrounding species ( $\text{F}^-$ ,  $\text{Cl}^-$  or  $\text{OH}^-$ ); however, the probability for  $\text{S}^{2-}$  to be incorporated into  
38 the apatite structure is highest for chlorapatite end-members.

39 Our results describe energetically feasible incorporation mechanisms for all three oxidations  
40 states of S ( $\text{S}^{6+}$ ,  $\text{S}^{4+}$ ,  $\text{S}^{2-}$ ) in apatite, along with structural distortion and concurring electronic  
41 structure changes. These observations are consistent with recently published experimental results  
42 (Konecke et al. 2017) that demonstrate  $\text{S}^{6+}$ ,  $\text{S}^{4+}$  and  $\text{S}^{2-}$  incorporation into apatite, where the ratio  
43 of  $\text{S}^{6+}/\sum\text{S}$  in apatite is controlled by oxygen fugacity ( $f\text{O}_2$ ). The new computational results  
44 coupled with published experimental data provide the basis for using S in apatite as a

45 geochemical proxy to trace variations in oxygen fugacity of magmatic and magmatic-  
46 hydrothermal systems.

47 **Keywords:** apatite, S incorporation, S oxidation state, energetics, geometry, column anion,  
48 lanthanum, oxybarometry

## 49 INTRODUCTION

50 Apatite group minerals, with the general chemical formula  $[\text{Ca}_{10}(\text{PO}_4)_6(\text{F},\text{Cl},\text{OH})_2]$ , are the  
51 most abundant phosphate minerals on Earth (Rakovan et al. 2013; Harlov 2015). The diverse  
52 chemistry of apatite is related to its flexible structure, which can accommodate a large number of  
53 cations and anions (Hughes and Rakovan 2002). The Ca cation sites can be replaced by alkali,  
54 alkali earth and transition metals (e.g., Na, Ba, Sr, Mn, Pb) and rare earth elements (e.g., La, Ce),  
55 whereas the major oxyanions such as  $\text{SiO}_4^{4-}$ ,  $\text{SO}_4^{2-}$ ,  $\text{CO}_3^{2-}$  can occupy the phosphate ( $\text{PO}_4^{3-}$ ) site  
56 (Hughes and Rakovan 2002).

57 Despite several studies demonstrating the evolution and variation of S recorded in apatite  
58 phases from igneous systems (Peng et al. 1997; Streck and Dilles 1998; Imai 2002; Parat et al.  
59 2002; Parat and Holtz 2004, 2005), little is known about the structure and thermodynamic  
60 stability of S in apatite. The recent study by Konecke et al. (2017) is the first to show  
61 qualitatively that variable abundances of  $\text{S}^{6+}$ ,  $\text{S}^{4+}$ , and  $\text{S}^{2-}$  are incorporated into apatite as  
62 crystallized from a mafic silicate melt under varying oxygen fugacity ( $f\text{O}_2$ ) conditions. The new  
63 experimental data on S redox chemistry in apatite highlight the need for theoretical  
64 understanding of the structural incorporation of different S species in apatite.

65 In this study, the thermodynamics and geometry of S incorporation in the apatite structure  
66 were investigated computationally. While common trace element impurities (e.g., Na, Si, REEs)  
67 in natural apatite are taken into account (Hughes et al. 1991), we focus on evaluating some of the  
68 most plausible scenarios that are consistent with experimental observations (e.g.,  $2\text{P}^{5+} \Leftrightarrow \text{S}^{6+} +$   
69  $\text{S}^{4+}$  and  $2(\text{F}^-, \text{Cl}^-, \text{OH}^-) \Leftrightarrow \text{S}^{2-} + \text{vacancy}$ ; Konecke et al. 2017). From a computational standpoint,  
70 each type of reactant and product must be treated independently, while the same system  
71 configuration and computational settings must strictly be applied for all species in a given  
72 chemical equation (Walker and Becker, 2015). In our approach, all phases considered are solids,  
73 and are quantum-mechanically modeled at ambient pressure (P) and temperature (T) conditions,  
74 because calculations at elevated P and T are currently beyond the capability for the applied  
75 approach. The relative stability of S with different oxidation states ( $\text{S}^{6+}$ ,  $\text{S}^{4+}$ , and  $\text{S}^{2-}$ ) in apatite is  
76 evaluated using balanced reaction equations, where the host apatite and the source phase for S  
77 (e.g., gypsum for  $\text{SO}_4^{2-}$  and troilite for  $\text{S}^{2-}$ ) are the reactants, and the S incorporated apatite and  
78 the sink phase that accommodates the replaced anions from apatite (e.g., monazite for  $\text{PO}_4^{3-}$ ) are  
79 the products. The host apatite, source, and sink phases are required for achieving a stoichiometric  
80 and balanced reaction equation. Thus, the reaction energy of the balanced equation indicates the  
81 stability of the S incorporated apatite, relative to coexisting solid phases. This computational  
82 evaluation permits the determination of: [1] the energetic favorability of S incorporation into  
83 apatite depending on substitutions required for charge balance, and [2] the electronic structure of  
84 atoms and the structural distortion of the incorporation site upon S incorporation. Based on the  
85 results of this study, chemical and crystallographic parameters that control the S incorporation  
86 into apatite are identified, and provide the computational and thermodynamic framework

87 required to investigate the potential role of S in apatite as a proxy to trace redox in magmatic  
88 systems.

## 89 PREVIOUS WORK

90 Historically, sulfate ( $S^{6+}$ ) has been suggested as the only oxidation state of S in the apatite  
91 structure (cf. Parat et al. 2011) based on the observation that S-rich (terrestrial) apatite,  
92 containing up to 0.8 wt.% S, exists in oxidizing (anhydrite-bearing) environments, where sulfate  
93  $S^{6+}$  and sulfite  $S^{4+}$  are the dominant (or only) S oxidation states in the melt and fluid, respectively  
94 (e.g., Rouse and Dunn 1982; Liu and Comodi 1993; Tepper and Kuehner 1999). Direct evidence  
95 for the presence of  $S^{6+}$  in the apatite structure was reported by Paris et al. (2001) who used  
96 synchrotron-radiation S *K*-edge micro X-ray absorption near-edge structure ( $\mu$ -XANES)  
97 spectroscopy to document the presence of sulfate in Durango apatite. Their results supported the  
98 hypothesis that S is incorporated as  $S^{6+}$  into the apatite structure. There are, however,  
99 experimental data from reduced systems, where sulfur is present mostly as sulfide ( $S^{2-}$ ) in the  
100 melt (Jugo et al. 2005), which suggests that apatite crystallizing from the melt may incorporate  
101  $S^{2-}$ . For instance, S concentrations in apatite from reduced lunar mare basalts (i.e., IW; iron-  
102 wüstite  $fO_2$  buffer; Sato et al. 1973) exceed 400  $\mu\text{g/g}$  S (Greenwood et al. 2011; Boyce et al.  
103 2014).

104 Recently, Konecke et al. (2017) provided qualitative evidence for the presence of  $S^{6+}$ ,  $S^{4+}$ ,  
105 and  $S^{2-}$  in apatite. Apatite crystals were crystallized from a hydrous, S-bearing mafic melt at  
106 1,000°C, 300 MPa, and over a broad range of oxygen fugacities ( $(\log(fO_2)) = \text{FMQ to FMQ}+3$ ;  
107 FMQ = fayalite-magnetite-quartz solid buffer). Those authors used S  $\mu$ -XANES to document the  
108 presence of distinct sulfate  $S^{6+}$  (absorption edge energy of  $\sim 2482$  eV), sulfite  $S^{4+}$  ( $\sim 2478$  eV) and

109 sulfide  $S^{2-}$  (~2470 eV) in the apatite structure (Figure 1). Specifically, apatite is dominated by  $S^{6+}$   
110 with a small contribution of  $S^{4+}$  under oxidizing conditions (FMQ+1.2 and +3); whereas  $S^{2-}$  is  
111 the dominant S oxidation state at more reducing conditions (FMQ). Their results demonstrate  
112 that once the S incorporation mechanism is determined, the S oxidation state in apatite may be  
113 used as a geochemical tool to quantify oxygen, and perhaps sulfur fugacity at redox conditions  
114 relevant to arc and MORB settings. However, the incorporation mechanisms and bonding  
115 environments of each S oxidation state in apatite remain unknown, and are imperative to the  
116 development of a quantitative S-in-apatite oxybarometer.

## 117 **METHODS**

### 118 **Computational parameters**

119 The computational approach adopted in this study is based on density functional theory (DFT)  
120 with planewaves representing functions for the overall wave function of upper valence and  
121 conduction band electrons (basis functions), while inner valence and core electrons of an atom  
122 and their interactions with the valence electrons are approximated using pseudopotentials. The  
123 optimization was performed using the quantum-mechanical code CASTEP (Segall et al. 2002).  
124 The Perdew-Wang generalized gradient scheme (GGA) was used in combination with ultrasoft  
125 pseudopotentials. The GGA scheme was parameterized by the Perdew–Burke–Ernzerhof (PBE)  
126 functional (Perdew et al. 1996). The energy cutoff for planewave expansion was 400.0 eV and  
127 the Brillouin zone was sampled using a k-point separation of  $0.05 \text{ \AA}^{-1}$ , according to the  
128 Monkhorst-Pack scheme (Monkhorst and Pack 1976). Self-consistent field cycles were assumed  
129 to converge with an energy difference of less than  $2.0 \times 10^{-6}$  eV/atom. A spin-polarized approach

130 was implemented when the unit cell of a mineral included atoms with unpaired spins. For  
131 example, ferrous iron, ( $\text{Fe}^{2+}$ ) has four 3d unpaired spins in its high-spin state. The electronic  
132 contribution of localized unpaired d states to materials properties may be incompletely described  
133 using standard DFT approaches. For such cases, a Hubbard U correction was implemented to  
134 account for the on-site Coulomb interaction (represented by the parameter,  $U$ ) and the exchange  
135 interaction ( $J$ ). For this approach, the effective Hubbard U parameter,  $U_{\text{eff}}$  ( $= U - J$ ) values, was  
136 adopted from previous studies investigating the Fe 3d states in various silicates ( $U_{\text{eff}} = 2.9$  and  
137 4.8; Hsu et al. 2011; Stackhouse et al. 2010) and sulfides ( $U_{\text{eff}} = 2.0$ ; Rohrbach et al. 2003).

### 138 **Incorporation energy calculation**

139 The reaction equation of S-incorporation consists of a pure (i.e., end-member) and impure  
140 (i.e., trace elements-bearing) apatite in the form of host apatite ( $\text{apatite}_{\text{host}}$ ) and S-incorporated  
141 apatite ( $\text{apatite}_{\text{S-incorporated}}$ ). Accordingly, appropriate solid sources for S ( $\text{source}_i$ ) and sinks for  
142 ions replaced in the mineral host ( $\text{sink}_i$ ) were selected to maintain stoichiometry. A host apatite  
143 phase and sources for S in different oxidation states are reactants, while S-incorporated apatite  
144 and sinks for anions being liberated from the apatite host are products. The general equation for  
145 this approach takes the form:



147 The incorporation reactions are balanced in order to involve one atom of S on both sides of  
148 the equation, such that the calculated reaction energy ( $E_{\text{rxn}}$ ) is defined as the energy required to  
149 incorporate one mole of S in an apatite host phase (unless otherwise stated). In addition, this

150 setup allows for a consistent quantum-mechanical treatment; i.e., using the same computational  
151 parameters throughout the equation, which is crucial to obtain reliable energetic data.

152 The role of a reaction medium, where an incorporation reaction occurs, can be important for  
153 computationally simulating incorporation into the mineral phase in geologically relevant systems.  
154 Examples for incorporation using solid sources and sinks can be found in Shuller et al. (2013,  
155 2014). The atomistic assessment for hydrated ions incorporated into host minerals is rather  
156 complicated and computationally difficult, as it involves a series of reaction equations that have  
157 to be combined in order to constrain species of different characters (hydrated vs. vacuum,  
158 charged vs. neutral, clusters vs. 3D periodic) in one net equation, while using a consistent  
159 approach (cf. Walker and Becker 2015; Smith et al. 2016). Additionally, it is more challenging to  
160 take into account the role of silicate melts or hydrothermal fluids under geologically relevant  
161 pressures and temperatures for a quantum-mechanical computational assessment of the  
162 incorporation process. Modeling magmatic-hydrothermal systems would require a quantum-  
163 mechanical molecular-dynamics simulation using large unit cells at high P-T conditions that  
164 approach or exceed the current limits of computational capability, and is otherwise beyond the  
165 scope of this study. Therefore, all source and sink phases are periodic solids, which commonly  
166 play a role in accommodating atoms that will be incorporated into and/or liberated from apatite.  
167 In order to increase the geological significance of our evaluation, minerals or ionic compounds  
168 that occur and are stable in magmatic or hydrothermal environments are selected as sources and  
169 sinks for the reaction equations. Once energies of all phases involved in the incorporation  
170 equations are computationally constrained, reaction energies for each incorporation equation can  
171 be calculated using the general approach:



172 
$$\Delta E_{rxn} = \sum E_{prod} - \sum E_{reac} \quad (2)$$

173 The resulting incorporation reaction energy indicates the stability of the S-incorporated  
174 apatite relative to the corresponding host apatite, and the source and sink phases. In addition, the  
175 relative stability of various incorporated apatite phases can be compared when common source  
176 phases are used. The incorporation energies calculated using CASTEP are well described by  
177 Shuller et al. (2013). Energies calculated using CASTEP include contributions from electronic  
178 properties such as electronic relaxations and spin-spin interactions. The  $\Delta E_{rxn}$  evaluated from the  
179 CASTEP energies of the reactants and products are in good agreement with enthalpies, for the  
180 reason that they are calculated at ambient pressure ( $VdP = 0$ ). To evaluate  $\Delta G_{rxn}$ , entropy  
181 contributions (e.g., vibrational entropies of the solid phases used in our study) must be  
182 considered. However, this requires significant computational efforts, and is outside the scope of  
183 this study.

184

### 185 **The structure model of apatite**

186 The initial models for the apatite end-members are adopted from the natural apatite structure,  
187  $[\text{Ca}_{10}(\text{PO}_4)_6(\text{F}, \text{OH}, \text{Cl})_2]$  ( $P6_3/m$ ; see Hughes et al. 1990; Hughes and Rakovan, 2015), and are  
188 depicted in Figure 2 and Figure S.1 (Supplemental material A). The column anion site [00z] of  
189 the apatite structure ( $P6_3/m$ ) is mainly occupied by  $\text{F}^-$ ,  $\text{OH}^-$ , and  $\text{Cl}^-$ . Natural apatite end-members  
190 are subdivided into fluorapatite  $[\text{Ca}_5(\text{PO}_4)_3\text{F}]$ , chlorapatite  $[\text{Ca}_5(\text{PO}_4)_3\text{Cl}]$ , and hydroxylapatite  
191  $[\text{Ca}_5(\text{PO}_4)_3(\text{OH})]$  based on a single occupant of the anion column, but often occur as a solid  
192 solution with binary or ternary anion columns (Hughes et al. 1990; Hughes and Rakovan 2002;

193 Hughes et al. 2016). The column anion site has the potential to accommodate other anions with  
194 different radii and/or charge. A well-known example is the incorporation of carbonate ( $\text{CO}_3^{2-}$ )  
195 into hydroxylapatite, which occurs in both the phosphate and column anion sites (Fleet and Liu,  
196 2007).

197 The apatite structure has two types of Ca sites as Ca1 and Ca2. The Ca1 type is coordinated  
198 to nine O atoms, while the Ca2 site is coordinated to six O atoms and one column anion. In the  
199  $\text{P6}_3/\text{m}$  space group, Ca2 atoms form triangles on the planes at  $z = 1/4$  and  $3/4$ . Each of the three  
200 Ca atoms at the triangle corners is bonded to the central anion in the  $[00z]$  column (Hughes et al.  
201 1990). Fluorine, the smallest of the column anions, is positioned on the mirror planes at  $z = 1/4$   
202 and  $3/4$  such that it is located at the center of the Ca triangle (Fig. 2a). The  $\text{OH}^-$  and  $\text{Cl}^-$  are too  
203 large to be positioned in the center of the Ca2 triangle, and are thus displaced above or below the  
204 planes. As a result of such displacement,  $\text{OH}^-$  and  $\text{Cl}^-$  have multiple possible positions along the  
205 anion column in the apatite unit cell (see Hughes, 2015). Since all atoms in the apatite structure  
206 are given full atomic occupancy in this study, the positions of  $\text{Cl}^-$  or  $\text{OH}^-$  below the planes at  $z =$   
207  $1/4$  and  $3/4$  were selected to complete the unit cell formula,  $[\text{Ca}_{10}(\text{PO}_4)_6(\text{F}, \text{Cl}, \text{OH})_2]$  (Fig. S.1).  
208 Thus, the chlorapatite and hydroxylapatite structures reduce the symmetry to the  $\text{P6}_3$  space group.  
209 Similar approaches to simulate hexagonal apatite without the  $m$  plane have been successfully  
210 tested in previous computational studies (e.g., Corno et al. 2006; Ulian et al. 2013). Using the  
211 structural and computational parameters above, a good agreement in the unit cell parameter  
212 values was found between calculated and natural end-member apatites reported by Hughes et al.  
213 (1989; see also Table 1 and Figure S.1). The resulting structures are then used to geometrically  
214 optimize the host and S-substituted apatite models (Fig. 3).

215 Energy-dependent density of states (DOS) analysis was performed to obtain the electronic  
216 structure of the apatite and S-bearing apatite configurations investigated in this study. Density of  
217 states analysis can be further delineated into partial density of states (PDOS) plots for certain  
218 angular momenta on atoms of interest (s, p, and d orbital characters in this study). The PDOS  
219 spectra of apatite configurations are consistent with a previous report on the electronic structure  
220 of Ca-phosphate crystals (Rulis et al. 2004). The electronic structure of non-S-bearing apatite  
221 and S-bearing apatite configurations are described in detail in Supplemental Material A.

222

### 223 **Sulfur replacement mechanisms in S-bearing apatite**

224 An important step in the incorporation energy calculations is to identify replacement  
225 mechanisms that may play a critical role in hosting S in natural apatite. All mechanisms tested in  
226 this study are based on previous reports of natural and experimentally produced apatite.

### 227 *Sulfate incorporation mechanisms*

228 It has been suggested that the P site is the most likely location where substitution of  $\text{SO}_4^{2-}$   
229 occurs in the apatite structure (Streck and Dilles 1998; Pan and Fleet 2002; Parat et al. 2011),  
230 where possible replacement mechanisms include:



233 In the current study, all calculations for  $\text{SO}_4^{2-}$  substitution are based on replacement  
234 mechanisms (3) and (4). We used geologically relevant solid source and sink phases for the

235 calculations. For instance, anhydrite ( $\text{CaSO}_4$ ) commonly coexists with S-rich apatite in oxidized  
236 magmatic systems (Baker and Ruther 1996a; Streck and Dilles 1998) and, thus, is a geologically  
237 relevant candidate as a source phase for  $\text{SO}_4^{2-}$ .

238 Moreover, in relatively oxidized magmatic systems (e.g., where the  $\text{S}^{6+}/\Sigma\text{S}$  ratio of the melt  
239 is  $> 0.5$ ),  $\text{Na}^+$  (replacing  $\text{Ca}^{2+}$ ) and  $\text{SiO}_4^{4-}$  (replacing  $\text{PO}_4^{3-}$ ) can be concomitant ions for  $\text{S}^{6+}$   
240 incorporation in apatite to maintain charge neutrality (Eq. 3 and 4). In addition, rare earth  
241 elements ( $\text{REE}^{3+}$ ) can substitute for  $\text{Ca}^{2+}$  in the apatite structure via the coupled substitutions  
242  $\text{REE}^{3+} + \text{Si}^{4+} \leftrightarrow \text{Ca}^{2+} + \text{P}^{5+}$  and  $\text{REE}^{3+} + \text{Na}^+ \leftrightarrow 2\text{Ca}^{2+}$  (Hughes et al. 1991; Pan and Fleet 2002).  
243 Hughes et al. (1991) reported a total  $\text{REE}^{3+}$  concentration range of 2 to 16 wt% in REE-bearing  
244 apatite samples and a good linear correlation between  $[\text{Na}^+ + \text{Si}^{4+}]$  vs.  $[\Sigma\text{REE}^{3+}]$  ( $\sim 1:1$  atomic  
245 ratio), which can be well explained by the coupled substitutions reactions above. Streck and  
246 Dilles (1998) reported variations in the S content in apatite, reaching up to 0.56 wt% S in apatite  
247 from the Yerington batholith (Nevada), and a strong correlation between  $[\text{Si}^{4+} + \text{Na}^+ - \Sigma\text{REE}^{3+}]$  vs  
248  $[\text{S}^{6+}]$  ( $\sim 1:1$  atomic ratio), which supports the coupled substitution of  $\text{Si}^{4+}$  and  $\text{Na}^+$  with  $\text{S}^{6+}$  and/or  
249  $\text{REE}^{3+}$ . Based on these considerations, La-bearing apatite is selected as the host apatite phase,  
250 which incorporates  $\text{SO}_4^{2-}$  in the structure. Two distinct scenarios involving La-bearing apatite,  
251  $[\text{Ca}_8\text{NaLa}][(\text{PO}_4)_6]\text{X}_2$  and  $[\text{Ca}_9\text{La}][(\text{PO}_4)_5(\text{SiO}_4)]\text{X}_2$ , are evaluated individually, and the effects of  
252  $\text{Na}^+$  and  $\text{Si}^{4+}$  on incorporating  $\text{SO}_4^{2-}$  into apatite are discussed in detail. Lanthanum-monazite  
253 ( $\text{LaPO}_4$ ), which commonly occurs as a P-bearing accessory mineral in igneous rocks (Foerster  
254 1998), is selected as a mineral sink phase for  $\text{PO}_4^{3-}$  being replaced by  $\text{SO}_4^{2-}$  in order to account  
255 the formation of La-bearing apatite. In models of *apatite<sub>host</sub>* (S-free) and *apatite<sub>S-incorporated</sub>*,  $\text{Na}^+$   
256 and  $\text{La}^{3+}$  are positioned on the Ca2 atomic sites at the mirror plane at  $z = 3/4$  and one of the three  
257  $\text{PO}_4^{3-}$  sites nearest to the column anion is replaced by  $\text{SiO}_4^{4-}$  or  $\text{SO}_4^{2-}$  (Fig. 2b and Fig. S.1).

258

259 *Sulfate and sulfite incorporation mechanisms*

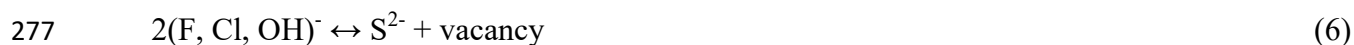
260 A recent study identified the co-existence of S<sup>4+</sup> and S<sup>6+</sup> in natural and experimentally  
261 produced apatite, and suggested a possible coupled substitution mechanism involving the  
262 replacement of two phosphate atoms by SO<sub>4</sub><sup>2-</sup> and SO<sub>3</sub><sup>2-</sup> via the coupled substitution (Konecke et  
263 al. 2017):



265 The plausibility of the proposed co-incorporation of S<sup>4+</sup> and S<sup>6+</sup> into fluor-, chlor-, and  
266 hydroxylapatite (eq. 5) is examined by balancing an incorporation reaction equation, in  
267 combination with the nickel-nickel oxide ( $\Delta\text{NNO}$ ) oxygen fugacity buffer (e.g., to simulate  
268 geologically relevant fO<sub>2</sub> conditions). A Na- and Si- apatite, [Ca<sub>7</sub>La<sub>2</sub>Na][(PO<sub>4</sub>)<sub>5</sub>(SiO<sub>4</sub>)](F, Cl,  
269 OH)<sub>2</sub>, is selected as the host phase. Anhydrite and La-monazite are used as source and sink  
270 phases, respectively. In models of *apatite*<sub>S-incorporated</sub>, one of the three nearest phosphate sites at  
271 the mirror plane at z = 1/4 and 3/4 to the anion column is replaced by SO<sub>3</sub><sup>2-</sup> and SO<sub>4</sub><sup>2-</sup>,  
272 respectively (see Fig. 2 and 3a).

273 *Sulfide incorporation mechanisms*

274 Henning et al. (2000) used single crystal X-ray diffraction to determine the structure of  
275 synthetic S<sup>2-</sup>-bearing apatite in the form Ca<sub>10</sub>(PO<sub>4</sub>)<sub>6</sub>S, and reported that S occupies the anion  
276 column via the following coupled substitution (Eq. 6):



278 Hence, a testable scenario for the incorporation of  $S^{2-}$  into the anion column in apatite  
279 involves FeS (troilite) and  $Na_2S$  as solid  $S^{2-}$  sources and is based on the affinity of  $Fe^{2+}$  and  $Na^+$   
280 for  $S^{2-}$  in geological processes (Fiege et al. 2015; Burns and Fyfe 1966). When  $F^-$  and  $Cl^-$  in  
281 apatite are replaced by  $S^{2-}$  from these sources, metal fluorides and chlorides are produced as a  
282 solid sink. To consider  $OH^-$  released from apatite, the metamorphic amphibole grunerite,  
283  $[Fe_7Si_8O_{22}(OH)_2]$ , is selected as a sink phase, while ferrosilite ( $FeSiO_3$ ) and quartz ( $SiO_2$ ) are  
284 added as reactants to balance the composition of grunerite. Grunerite, as a key amphibole end-  
285 member, possesses a broad stability field in the simple system of  $FeO-SiO_2-H_2O$  (Lattard and  
286 Evans, 1992). Thermodynamic equilibria between grunerite and other Fe-silicates, such as  
287 ferrosilite and fayalite, have been adopted as a tool to estimate temperature, pressure, and  $H_2O$   
288 activity in metamorphic, hydrothermal, and volcanic systems (e.g., Lattard and Evans 1992;  
289 Elliott 2001). This makes it a suitable phase to investigate magmatic and magmatic-hydrothermal  
290 scenarios.

291 When building initial models (i.e., ones subjected to geometry optimization),  $S^{2-}$  replaces two  
292  $F^-$ ,  $Cl^-$ , or  $OH^-$  anions in fluor-, chlor- or hydroxylapatite (Eq. 6). Once placed in the column,  $S^{2-}$   
293 can be re-positioned to any unoccupied position of the column during the course of the geometry  
294 optimization. The optimization algorithm calculates local minima in the energy landscape by  
295 adjusting the lattice parameters, and the coordinates of each atom within the initial model.  
296 Therefore, it is important to ensure an energetic or geometric variation in the optimization result  
297 as the initial position of  $S^{2-}$  varies in the anion column. The position of  $F^-$ ,  $Cl^-$  and  $OH^-$  in the  
298 apatite anion column (i.e., (00z) calculated from the end-member apatite; see Table 1) is selected  
299 as the position of  $S^{2-}$  in the initial models. Where necessary, initial  $S^{2-}$  is referred to as  $S(F, Cl,$   
300  $OH)_{ini}$ , when a position near the anion column is chosen as the initial  $S^{2-}$  position replacing  $F^-$ ,  $Cl^-$ ,

301 or OH<sup>-</sup> anions. For this type of replacement, full incorporation of S<sup>2-</sup> in apatite is considered in  
302 the form of Ca<sub>10</sub>(PO<sub>4</sub>)<sub>6</sub>S. Moreover, we considered the partial incorporation of S<sup>2-</sup> in the 1×1×2  
303 supercell of apatite in the form of Ca<sub>20</sub>(PO<sub>4</sub>)<sub>12</sub>S(F, OH or Cl)<sub>2</sub> (Fig. 3b). Notably, in the supercell,  
304 a S<sup>2-</sup> atom is located between two of column anions such that the optimized positions of the  
305 column anions are the result of S<sup>2-</sup> interacting with surrounding F<sup>-</sup>, Cl<sup>-</sup>, or OH<sup>-</sup> anions. The  
306 calculated reaction energy defines the energy required for the incorporation of one S<sup>2-</sup> ion in the  
307 1×1×2 supercell of apatite.

308

### 309 **Computational scopes and errors**

310 In a computational study like this, the sources of errors have more of a systematic character  
311 and less of a random one as they occur in experimental studies. One source of variability is the  
312 computational parameters, such as density functionals, pseudopotentials, as well a quantity and  
313 types of basis functions. Testing all parameters for the examples used in this study would  
314 increase the computational effort by at least an order of magnitude. Therefore, testing can be  
315 done only with a limited number of examples and computational parameters. Importantly, we  
316 concluded that the energy for stoichiometric reaction equations may be minimally susceptible to  
317 the DFT functional chosen for calculation, as long as all computational parameters are consistent  
318 within such equations. For example, two sets of the incorporation energy data for an  
319 incorporation reaction equation were produced using the GGA scheme parameterized with the  
320 PBE and the PerdewWang1991 (PW91) functional (the reaction equation in Table S.1 in  
321 Supplemental Material A concerns all three different monovalent column anions). Although the  
322 energy of respective mineral phase differs by up to a few tens of eV, the incorporation energy

323 difference of calculation using the PBE and PW91 is only on the order of  $\sim 0.015$  eV (or  $\sim 1.5$   
324 kJ/mol) and the relative stability among the apatites remain unchanged.

325 More important than such parameter testing is a good understanding of the limitations of the  
326 model setup. This includes the structural model setup with a limited-sized unit cell, which  
327 increases the relative concentration of the incorporated species, as well as the decision to use  
328 selected solid source and sink phases. All of these decisions have been made to model  
329 geologically relevant scenarios in reasonable computation times. Our approach is suitable to  
330 learn about the thermodynamic stability with respect to references, and the atomic and electronic  
331 structure of mineral phases. The thermodynamic energies of incorporation are relative quantities  
332 that would change by choosing different sink/source phases or transitioning to dynamic  
333 hydrothermal fluids, whereas the results for the electronic/atomic structure of incorporation  
334 would remain unaffected.

335

336

## RESULTS

### Incorporation energy and geometry

338

#### *Sulfate ( $SO_4^{2-}$ )*

339 The reaction equations and energies for  $S^{6+}$  incorporation into La-apatite phases are  
340 presented in Table 2. In the equations, charge imbalance of  $La^{3+}$  in place of  $Ca^{2+}$  is compensated  
341 by coupled substitution with  $Na^+$  or  $Si^{4+}$  in the apatite structure. Incorporation energies  
342 calculated from the Na-bearing apatite phases are lower than those of the Si-bearing phases for



343 all tested scenarios. In the Na-bearing system, the lowest incorporation energy is found in  
344 fluorapatite, followed by chlorapatite and hydroxylapatite. Energy differences between those are  
345 relatively small (3 to 6 kJ/mol). In the Si-bearing apatite, the incorporation of  $S^{6+}$  into  
346 chlorapatite is energetically more favored than the incorporation into fluorapatite and  
347 hydroxylapatite (by 10.4 kJ/mol).

348 The unit cell volume is changed as a function of cell parameters and, thus, can be indicative  
349 of the net effect of replacing phosphate by  $SO_4^{2-}$  in the optimized structure. The cell volumes of  
350 S-incorporated apatite phases are presented in Table 3. Exchange of  $P^{5+} + Ca^{2+} \leftrightarrow S^{6+} + Na^+$  and  
351 of  $2P^{5+} \leftrightarrow S^{6+} + S^{4+}$  in the unit cell of fluor-, chlor-, and hydroxylapatite leads to a volume  
352 expansion by 3 to 5 and 6 to 8  $\text{\AA}^3$ , respectively. The ionic radius of 4-coordinated  $S^{6+}$  (0.12  $\text{\AA}$ ) is  
353 smaller than that of  $P^{5+}$  (0.17  $\text{\AA}$ ; Shannon, 1976). Thus, the volume expansion by the coupled  
354 exchanges should be mainly due to the larger ionic size of  $Na^+$  compared to  $Ca^{2+}$ , and  $Si^{4+}$   
355 compared to  $P^{5+}$ . Cations occupying the Ca2 site are 7-coordinated, and the size of 7-coordinated  
356  $Na^+$  and  $Ca^{2+}$  are approximately 1.12 and 1.06  $\text{\AA}$ , respectively. The 4-coordinated  $Si^{4+}$  is 0.26  $\text{\AA}$   
357 and thus its occupancy in place of  $P^{5+}$  would lead to a volume expansion of the unit cell.  
358 Although, accounting for less than 1.4 % of the unit cell volume, such a variation in the unit cell  
359 volume shows a monotonic increase with increasing column anion size ( $Cl^- > OH^- > F^-$ ) in the  
360  $S^{6+}$  incorporated Si-bearing apatite series.

361 In the optimized  $S^{6+}$  incorporated Na- and Si-bearing apatite phases, bond lengths and angles  
362 measured from incorporated  $SO_4^{2-}$  molecules are similar to reported values for the  $SO_4^{2-}$   
363 molecule (109.5° and 1.49  $\text{\AA}$ ) with a maximum deviation of 2.7° and 0.02  $\text{\AA}$ . The nearest  $PO_4^{3-}$   
364 and  $SO_4^{2-}$  to the column site have two O atoms displaced above and below the planes at  $z = 1/4$

365 and 3/4 while the other two O atoms are placed on the planes (Fig. 4a). The former two O atoms  
366 face toward S on the (0 0 z) column anion such that their positions may be more susceptible to  
367 the property of the column ion than the latter two. The angle formed between the S center and  
368 the column-oriented O atoms (O-S-O) are presented in Fig. 4a and Table 3. In the  $S^{6+}$   
369 incorporated Na-bearing apatite series, the O-S-O angle tends to increase with increasing column  
370 anion size from  $107.9^\circ$  to  $108.4^\circ$  whereas the O-P-O angle in fluorapatite changes from  $107.2^\circ$   
371 (X = F) to  $107.7^\circ$  in chlorapatite (Table 3).

372

### 373 *Sulfate ( $SO_4^{2-}$ ) and sulfite ( $SO_3^{2-}$ )*

374 The reaction equations and energies for co-incorporation of sulfite ( $S^{4+}$ ) with sulfate ( $S^{6+}$ )  
375 into La-bearing fluor-, chlor-, and hydroxylapatite are presented in Table 2. In the reaction, La-  
376 monazite ( $LaPO_4$ ) is used as a sink phase to accommodate phosphate released from the host  
377 apatite. Solid nickel ( $Ni_{(s)}$ ) is introduced to play a role as an oxygen buffer to take up one O atom  
378 of the sulfate  $SO_4^{2-}$  molecule forming a sulfite  $SO_3^{2-}$  molecule (reduction of  $S^{6+}$  to  $S^{4+}$ ). The  
379 molecular geometry of  $SO_3^{2-}$  is a trigonal pyramid with a lone pair of electrons at one corner. As  
380 mentioned above, two of the four  $PO_4^{3-}$  (or  $SO_4^{2-}$ ) O atoms are displaced from the planes at  $z =$   
381  $1/4$  and face toward the (0 0 z) anion column. The other two are placed on the plane and face  
382 away from the column (Fig. 4a). In building a model for  $SO_3^{2-}$  replacing  $PO_4^{3-}$ , one of either the  
383 former two or the latter two O atoms is replaced by a lone pair of electrons (Fig. 4b and c). In  
384 Figure 4 and Table 2, the two cases are labeled A-type and B-type  $SO_3^{2-}$ , respectively.

385 The incorporation energy is the lowest in chlorapatite compared to fluorapatite and  
386 hydroxylapatite, and the energy difference between the former and the latter two are 19 kJ/(1 mol

387  $\text{SO}_3^{2-} + 1 \text{ mol SO}_4^{2-}$ ) and 22 kJ/(1 mol  $\text{SO}_3^{2-} + 1 \text{ mol SO}_4^{2-}$ ), respectively (Table 2). The  
388 orientation of the  $\text{SO}_3^{2-}$  loan pair influences the stability of the incorporated apatite. Lower  
389 incorporation energy is found for A-type  $\text{SO}_3^{2-}$ -incorporated apatite when compared to B-type  
390  $\text{SO}_3^{2-}$ -incorporated apatite (the energy difference is 14 to 16 kJ/(1 mol  $\text{SO}_3^{2-} + 1 \text{ mol SO}_4^{2-}$ ) for  
391 each apatite end-member). Thus, the co-incorporation mechanism of sulfate and A-type sulfite is  
392 energetically more likely than the mechanism involving B-type sulfite.

393 In the optimized S-incorporated apatite phases, bond lengths and angles measured from the  
394 incorporated  $\text{SO}_3^{2-}$  molecules are in good agreement with previous reported values (104.3° and  
395 1.53 Å) (Andersen and Lindqvist, 1984). The cell volumes and distances between  $\text{S}^{4+}$  and  $\text{F}^-$ ,  $\text{Cl}^-$ ,  
396 or  $\text{OH}^-$  in optimized S-incorporated apatite phases are presented in Table 4. Larger cell volumes  
397 are found for B-type  $\text{SO}_3^{2-}$ -incorporated apatite when compared to A-type  $\text{SO}_3^{2-}$ -incorporated  
398 apatite. B-type  $\text{SO}_3^{2-}$ -incorporated apatite has 0.05 to 0.2 Å longer (F, Cl, OH)– $\text{S}^{4+}$  and (F, Cl,  
399 OH)– $\text{S}^{6+}$  distances than A-type  $\text{SO}_3^{2-}$  apatite. The cell volume results coincide with the (F, Cl,  
400 OH)–S distance variation in the sense that the longer atomic distance generally contributes to the  
401 larger cell volume of the mineral. The calculated z fractional coordinate of the S center of  $\text{SO}_4^{2-}$   
402 is barely displaced from the plane at  $Z = 3/4$  ( $< 0.03$  Å). The S atom of A-type  $\text{SO}_3^{2-}$  is displaced  
403  $\sim 0.2$  Å from the plane at  $Z = 1/4$  whereas the B-type  $\text{SO}_3^{2-}$  deviates by less than 0.05 Å from the  
404 same plane.

#### 405 *Sulfide ( $\text{S}^{2-}$ )*

406 The equations and calculated energies of reactions for  $\text{S}^{2-}$  incorporation into fluor-, chlor-,  
407 and hydroxylapatite in the Fe-S and Na-S, and Fe-Si-S systems are presented in Table 5. Lattice  
408 parameters of the initial and optimized  $\text{S}^{2-}$  incorporated apatite structures are summarized in

409 Table 6. The calculated reaction energies for  $S^{2-}$  incorporation are highly dependent on selected  
410 source and sink phases. Energies calculated by using Fe-bearing phases (Fe-S system) are higher  
411 than incorporation energies calculated using Na-bearing phases (Na-S system). This effect arises  
412 from the higher stability of troilite (FeS) used as a source phase relative to Fe-bearing sink phase  
413 solids than the stability of  $Na_2S$  relative to Na sink phases. However, in a given system, where  
414 source phases and/or sink phases are fixed, the stability of S-incorporated apatite phases can be  
415 evaluated relative to host apatite phases. In case of hydroxylapatite, because Si-bearing minerals  
416 are used as source phases in addition to FeS, the stability of apatite phases is not comparable  
417 between the Fe-S and Fe-Si-S systems. Full incorporation of  $S^{2-}$  into the Cl site (denoted by  
418  $S(Cl)_{ini}$  in Table 5) of chlorapatite is more stable than into the F site ( $S(F)_{ini}$ ) of fluorapatite. The  
419 calculated incorporation energy difference between fluorapatite and chlorapatite is 256 and 265  
420 kJ/mol in the Fe-S and Na-S systems, respectively. Full incorporation of  $S^{2-}$  into the  
421 hydroxylapatite structure achieves appreciable stability relative to Fe-silicates (-71.9 kJ/mol;  
422 Table 5).

423 The optimized structures of fully  $S^{2-}$  incorporated apatite are compared with a previous study  
424 of synthetic sulfoapatite,  $[Ca_{10}(PO_4)_6S]$  (Henning et al. 2000; Table 6). Calculated cell  
425 parameters are in good agreement with the measured parameters. In the optimized structure of  
426  $S^{2-}$  full incorporation, the position of  $S^{2-}$  is at  $z = 0.5018$  and  $0.5004$  in the hydroxylapatite and  
427 chlorapatite structures, respectively and at  $z = 0.75$  in the fluorapatite structure where  $F^-$  is  
428 replaced by  $S^{2-}$  in the initial model. When located at  $(0, 0, 0.70)$  in the initial model of  
429 fluorapatite, however,  $S^{2-}$  is relaxed to the position at  $z = 0.5$  during geometry optimization,  
430 resulting in the incorporation energy lower than one having  $S^{2-}$  at  $z = 0.75$  (the energy difference  
431 of 129 kJ/mol) (Table 5 and 6). This indicates that  $S^{2-}$  in the  $F^-$  position ( $z = 1/4$  or  $3/4$ , at the

432 center of the Ca triangle) is metastable for  $S^{2-}$  larger than  $F^-$ , and (0, 0, 0.5) is the most likely  
433 position of column anion  $S^{2-}$  in sulfoapatite,  $[Ca_{10}(PO_4)_6S]$ . This result is in good agreement with  
434 experimental data for synthetic sulfoapatite ( $z = 0.5$ ) (Henning et al. 2000).

435 Lower reaction energies are found in cases of partial incorporation into chlorapatite when  
436 compared to those of fluorapatite (Table 5). The incorporation energy also depends on where  $S^{2-}$   
437 is incorporated in the anion column of the initial model structure (denoted by  $(F, Cl, OH)_{ini}$  in  
438 Table 6). Upon the partial incorporation into fluorapatite,  $S^{2-}$  on a  $F^-$  position ( $S(F)_{ini}$ ) is less  
439 stable than  $S^{2-}$  on  $Cl^-$  and  $OH^-$  positions ( $S(Cl)_{ini}$  and  $S(OH)_{ini}$ ) (energy difference of 55 to 56  
440 kJ/mol). When partially incorporated into chlorapatite, the dependence of the S stability on the  
441 column position is relatively lower and leads to energy differences between  $S(F, Cl, OH)_{ini}$  less  
442 than 6 kJ/mol. From these results, one can infer that the probability of  $S^{2-}$  being incorporated into  
443 apatite is enhanced when  $S^{2-}$  is partitioned into the Cl-bearing apatite structure or when Cl  
444 coexists with  $S^{2-}$  in the anion column site. Upon partial substitution of  $S^{2-}$  in hydroxylapatite, the  
445 stability of incorporated  $S^{2-}$  is higher at the Cl or OH site relative to the F site.

446 Column anion positions in the optimized structures of partially  $S^{2-}$  substituted apatite are  
447 depicted in Figure 5. The anion column S is located at  $z = 0.57$  in the optimized structure of  
448 fluorapatite when  $S^{2-}$  is initially positioned at the  $Cl^-$  or  $OH^-$  site (denoted by  $(F, Cl, OH)_{ini}$  in  
449 Table 6). The minimum energy configurations are found when the position of  $S^{2-}$  is (0, 0, 0.61)  
450 in the hydroxylapatite structure. The anion column  $S^{2-}$  is positioned at  $z = 0.51$  in  $S^{2-}$   
451 incorporated chlorapatite, regardless of its initial position. Interaction with surrounding column  
452 anions is an important factor that determines the position of  $S^{2-}$ . In the anion column  
453 environment tested here where S is located between two anions—i.e.  $F^-$ ,  $Cl^-$ , or  $OH^-$ , at or near  $z =$

454 1/4 and 5/4 (with respect to the initial 1×1×1 unit cell) in the 1×1×2 supercell (Fig. 5) –the  
455 lowest-energy configuration shows that S<sup>2-</sup> in the anion column is located at z = 0.50 to 0.61.  
456 The presence of S<sup>2-</sup> in the anion column results in displacing the remaining F<sup>-</sup>, Cl<sup>-</sup>, or OH<sup>-</sup> above  
457 or below the planes at z = 1/4.

458

459

## DISCUSSION

### 460 **Parameters that control the sulfur oxyanions (SO<sub>4</sub><sup>3-</sup> and SO<sub>3</sub><sup>2-</sup>) incorporation into apatite**

461 Generally, higher reaction energies result from stable reactants or unstable products.  
462 Therefore, the lower S<sup>6+</sup> incorporation energies observed for the La-Na-bearing apatite when  
463 compared to La-Si-bearing apatite (Table 2) indicate that (i) the La-Si-bearing host apatite is  
464 more stable than La-Na-bearing host apatite or (ii) that S<sup>6+</sup> incorporation into apatite becomes  
465 energetically more stable when SO<sub>4</sub><sup>2-</sup> is coordinated with Na<sup>+</sup> and PO<sub>4</sub><sup>3-</sup> than with Ca<sup>2+</sup> and  
466 SiO<sub>4</sub><sup>4-</sup>. The incorporation energies of La<sup>3+</sup> and Na<sup>+</sup> versus La<sup>3+</sup> and Si<sup>4+</sup> into apatite were  
467 calculated in order to consider the stability of the impure apatite hosting S oxidation states  
468 relative to the pure end-member fluor-, chlor-, and hydroxylapatite (Table 7). Incorporation  
469 energies of La<sup>3+</sup> and Na<sup>+</sup> into apatite are higher than those of La<sup>3+</sup> and Si<sup>4+</sup> into apatite for  
470 fluorapatite and hydroxylapatite. Hence, scenario (i) may be favored for fluorapatite and  
471 hydroxylapatite. Scenario (ii) can be evaluated using linear combinations of equations for S<sup>6+</sup>  
472 incorporation into La<sup>3+</sup>-bearing apatite (Table 2) and for La<sup>3+</sup> incorporation into end-member  
473 apatite (Table 7). The incorporation energies of S<sup>6+</sup> and Na<sup>+</sup>-bearing apatite are lower than those  
474 of S<sup>6+</sup> and Si<sup>4+</sup>-bearing apatite for all apatite end-members, which supports scenario (ii). In

475 addition, comparison between equations for  $S^{6+}$  incorporation into host apatite phases (Table 2  
476 and 7) suggests that incorporation of  $SO_4^{2-}$  into La-bearing apatite may be energetically more  
477 favorable than the incorporation into the end-member fluor-, chlor-, and hydroxylapatite.

478 Since replacements of  $Ca^{2+}$  and  $PO_4^{3-}$  by other ions ( $Na^+$ ,  $La^{3+}$ ,  $SiO_4^{4-}$  and  $SO_4^{2-}$ ) are made at  
479 the nearest position to the column anions (F, Cl, OH) in all models tested, it is expected that  
480 energy differences among fluorapatite, chlorapatite, and hydroxylapatite used as reactants and  
481 products arise mainly from chemical or structural environments on the column anion sites (Fig.  
482 2). In this regard, the first and second possibilities above ((i) and (ii)) can be understood in terms  
483 of interatomic interactions. In host and S-incorporated apatite, the Ca2 triangle that surrounds the  
484 column anion has one or two  $Ca^{2+}$  ions replaced by  $Na^+$  or  $La^{3+}$  (Fig. 2b). Cations positioned at  
485 the triangle corners are electrostatically repelled from each other and attracted to the column  
486 anion and surrounding phosphate and other oxyanions. The Coulomb energy between the  
487 interacting ions is defined in a classical manner such that the energy is proportional to the  
488 product of the charges of the two ions,  $q_i$  and  $q_j$ , and increases inversely with the distance  
489 between the two,  $r_{ij}$ . When multiple atoms are present in a system, the Coulomb energy is  
490 defined as Equation 7.

$$491 \quad E_{\text{coulomb}} = \frac{e^2}{4\pi\epsilon_0} \sum_{i>j} \frac{q_i q_j}{r_{ij}} \quad (7)$$

492 Here, the Coulomb force of the cations in a triangle involves two contributions: (i) repulsion  
493 between the cations and (ii) attraction of the triangle cations with the surrounding anions. A  
494 higher repulsive force is exerted on the triangle structure when  $La^{3+}$  is located at a corner of the  
495 triangle than when  $Na^+$  or  $Ca^{2+}$  is there. In this case, the effect of  $La^{3+}$  ion can be counteracted by  
496 coexistence with  $SiO_4^{4-}$  that makes the triangle less unstable. That is, the attractive coulombic

497 force between cations and  $\text{SiO}_4^{4-}$  with a 4- charge is stronger than the force exerted by  $\text{PO}_4^{3-}$  with  
498 a 3- charge. This indicates that La-bearing apatites can be stabilized by coexisting with silicate  
499 ions (the first possibility above). On the other hand, the presence of  $\text{Na}^+$  or  $\text{SiO}_4^{4-}$  near  $\text{SO}_4^{2-}$  can  
500 make a large contribution to the stability of  $\text{S}^{6+}$ -incorporated apatites.  $\text{Na}^+$  is electrically less  
501 attractive to  $\text{SO}_4^{2-}$  than  $\text{Ca}^{2+}$  while  $\text{SiO}_4^{4-}$  is more repulsive to  $\text{SO}_4^{2-}$  than  $\text{PO}_4^{3-}$ . This means that  
502 electrical interaction of  $\text{SO}_4^{2-}$  with  $\text{Na}^+$  or  $\text{SiO}_4^{4-}$  alone does not increase the stability of  
503 incorporated  $\text{SO}_4^{2-}$ . However,  $\text{Na}^+$  on the Ca2 site and  $\text{SiO}_4^{4-}$  on a neighboring phosphate site  
504 both can contribute to energy lowering of the anion column triangle.  $\text{Na}^+$  occupying the Ca2 site  
505 has a lower repulsive force than  $\text{Ca}^{2+}$ , which lowers the instability of the triangular arrangement  
506 by cation-cation repulsion. The presence of a neighboring silicate anion will counteract the  
507 repulsive force between the triangle  $\text{Ca}^{2+}$  ions. However the effect of  $\text{SiO}_4^{4-}$  on  $\text{Ca}^{2+}$  ions will be  
508 less than the case of  $\text{La}^{3+}$  included in the host apatite. The net effect of these contributions might  
509 enable some of the S-incorporated apatites to be more stable in the coexistence with  $\text{Na}^+$  than  
510 with  $\text{Si}^{4+}$  (the second possibility).

511 The effect of the anion column on  $\text{S}^{6+}$  incorporation into La-bearing apatite is more  
512 pronounced in the Si-bearing apatite system when compared to the Na-bearing apatite system.  
513 That is, the Si-bearing system shows greater differences in the incorporation energies among the  
514 apatite end members than the Na-bearing system (Table 2). In the former system, the lowest  
515 incorporation energy is found for chlorapatite, followed by fluorapatite and hydroxylapatite. The  
516 repulsive force between  $\text{SO}_4^{2-}$  and column anion  $\text{F}^-$ ,  $\text{OH}^-$  or  $\text{Cl}^-$  is one possible contribution to the  
517 stability of  $\text{S}^{6+}$ -incorporated apatite. In the optimized S-incorporated apatite, the center-to-center  
518 distance is 3.55 Å between  $\text{F}^-$  and  $\text{S}^{6+}$ , 3.92 Å between  $\text{Cl}^-$  and  $\text{S}^{6+}$  and 3.61 Å between  $\text{OH}^-$  and



519  $S^{6+}$  (Table 3). Therefore, chlorapatite is expected to experience the smallest repulsive force  
520 between the column anion ( $Cl^-$ ) and  $SO_4^{2-}$ .

521 The lower energy of co-incorporation of  $S^{4+}$  with  $S^{6+}$  into the La-bearing apatite is found for  
522 chlorapatite when compared to fluor- and hydroxylapatite (Table 2). This may again be attributed  
523 to the longest distance and thus the lowest repulsive force between the sulfur oxyanions and  
524 column anion  $Cl^-$  compared to  $F^-$  and  $OH^-$  (Table 4). The stability of sulfite-substituted apatite  
525 can be affected by the geometry mismatch with the phosphate site (trigonal pyramid vs  
526 tetrahedron). Differences in incorporation energy and geometry between apatites with A- and B-  
527 type  $SO_3^{2-}$  indicate that the oxygen site replaced by the lone pair electron of  $SO_3^{2-}$  can cause local  
528 defects in the apatite structure and govern the stability of sulfite that substitutes the phosphate  
529 site (Table 2 and Figure 3).

530 In summary, the relative stability of incorporated  $SO_4^{2-}$  and/or  $SO_3^{2-}$  into apatite can depend  
531 on accompanying trace elements and the column anion. The replacement energies in Table 2  
532 suggest that when  $La^{3+}$  and  $PO_4^{3-}$  are replaced by  $Ca^{2+}$  and  $SO_4^{2-}$ , it is more energetically  
533 favorable to do this in a system that compensates for the  $La^{3+}$  charge by replacing  $Ca^{2+}$  by  $Na^+$   
534 rather than  $PO_4^{3-}$  by  $SiO_4^{4-}$ . The relative stability for the sulfur oxyanion substituted into  
535 chlorapatite is greater than ones for fluorapatite and hydroxylapatite. The orientation of the  
536 sulfite molecule can matter upon substitution with the phosphate site in apatite unlike sulfate  
537 with the identical molecular geometry with phosphate.

### 538 **Effect of site preference of trace elements on sulfur substitution into apatite**

539 Site preference of atoms is important in understanding the crystal chemical behavior of trace  
540 elements that substitute for the Ca sites in apatite (Fleet and Pan 1995).  $Na^+$  has been found to

541 occupy both Ca1 and Ca2 sites, but has a strong preference for the Ca1 site (Hughes et al. 1991;  
542 Fleet and Pan 1995; Rakovan and Hughes 2000). REE including La<sup>3+</sup> generally tend to occupy  
543 the Ca2 site (Hughes et al. 1991). For consistency, we selected the Ca2 site that is closer to the  
544 column anion than the Ca1 site, for the position of both Na<sup>+</sup> and La<sup>3+</sup>, although this site is rather  
545 uncommon for Na<sup>+</sup> in natural apatite. One important question is whether the site preference of  
546 neighboring trace elements may influence the energetics and geometry of sulfur incorporation  
547 into apatite. As an example, incorporation energy of sulfate into the La-Na bearing apatite is  
548 calculated considering the site preference of Na<sup>+</sup> between the Ca1 and Ca2 site (Table 8). Na<sup>+</sup> is  
549 swapped between the Ca1 and Ca2 site (denoted by S' and S'' in Fig. S.1a and b) in the model  
550 configuration of S<sup>6+</sup> incorporated fluor- and chlorapatite. The incorporation energy of S<sup>6+</sup> into  
551 La-bearing apatite decreases by 2.1 and 9.0 kJ/mol for fluor- and chlorapatite, respectively, as  
552 Na<sup>+</sup> is positioned at the Ca1 site than at the Ca2 site (compare with the equivalent reaction  
553 equation and energy in Table 2). The energies required to exchange Na<sup>+</sup> between the Ca2 and  
554 Ca1 site of apatite in the form of [Ca<sub>9</sub>Na][(PO<sub>4</sub>)<sub>5</sub>(SO<sub>4</sub>)]X<sub>2</sub> (X = F and Cl) are negative, indicating  
555 increase in the stability of SO<sub>4</sub><sup>2-</sup> incorporated apatite with Na<sup>+</sup> positioned at the Ca1 site (Table  
556 8). These results support that the site preference of elements in the apatite structure is an  
557 important factor in predicting the stability of sulfur incorporated apatite. Future research could be  
558 aimed at systematic investigation for the role of site preference of trace elements on sulfur  
559 incorporation into apatite.

560

## 561 Sulfide ( $S^{2-}$ ) site stability in the apatite structure

562 The incorporation energy of  $S^{2-}$  into apatite is closely correlated with the optimized structure  
563 of S-bearing apatite. Full or partial substitution of  $S^{2-}$  into fluor-, chlor-, or hydroxylapatite  
564 results in lower incorporation energies when  $S^{2-}$  is positioned in the  $Cl^-$  and  $OH^-$  site relative to  
565 the  $F^-$  site (Table 5 and 6). The occupancy of  $S^{2-}$  at (0, 0, 0.75) results in an increase in the Ca-Ca  
566 distance in the  $Ca_2$  triangle at  $z = 3/4$  by  $\sim 10\%$ . Such structural alteration by S on the F site can  
567 significantly contribute to higher incorporation energy when compared to  $S^{2-}$  incorporation on  
568 the  $Cl^-$  and  $OH^-$  site. It is inferred that the substitution of  $S^{2-}$  on the  $F^-$  site in the apatite structure  
569 is energetically and geometrically less likely. In the lowest-energy configurations for the partial  
570 substitution, the predicted position of the  $S^{2-}$  ion in fluor-, chlor- and hydroxylapatite is 1 to  
571  $1.6 \text{ \AA}$  displaced from the mirror plane at  $z = 1/4$  or  $3/4$  (Fig. 5 and Table 6), which is close to the  
572  $Cl^-$  site in the natural apatite structure ( $0.182$  displacement in the  $z$  value from the mirror planes;  
573 Table 1). These results suggest that the  $Cl^-$  site can be one of the energetically stable sites for  $S^{2-}$   
574 incorporation in the apatite structure.

575 The relative stability of a substituent ion in an atomic site of a mineral structure can be  
576 explained on the basis of the Goldschmidt's substitution rules, which states that the "native" ions  
577 in a given site are more likely to be substituted by foreign ions with a similar radius, charge, and  
578 ionic nature (e.g., chemical hardness and electronegativity; Klein et al. 2002). The reported ionic  
579 radii of  $F^-$ ,  $Cl^-$ , and  $S^{2-}$  are  $1.33$ ,  $1.81$ , and  $1.84 \text{ \AA}$ , respectively (Shannon, 1976). The ionic radius  
580 of  $S^{2-}$  is very close to that of  $Cl^-$  (difference by  $1.6\%$ ) whereas there is an appreciable difference  
581 in ionic radius between  $S^{2-}$  and  $F^-$  anions by  $27.7\%$ . This confirms that incorporation of  $S^{2-}$  on  
582 the  $F^-$  site is rather unlikely. In addition,  $S^{2-}$  is similar in its chemical nature to  $Cl^-$ . The chemical

583 hardness of  $S^{2-}$  is classified as a soft base, which gives rise to its affinity with various soft  
584 transition metals such as  $Fe^{2+}$ ,  $Cu^+$ , and  $Hg^{2+}$  in geological processes, e.g., ore-formation  
585 (Pearson 1968). Chlorine is chemically soft and less electronegative than fluorine. Such chemical  
586 similarities between  $S^{2-}$  and  $Cl^-$  may contribute to affinity of the two anions in apatite.

587

### 588 **Future work**

589 As  $H_2S$  in a silicate melt is deprotonated,  $S^{2-}$  may be partitioned into mineral phases as either  
590  $S^{2-}$  or  $HS^-$ . The possibility of  $HS^-$  incorporation into apatite was not addressed in this study  
591 because the results of Henning et al. (2000) already indicate that  $S^{2-}$  may be the favored S species,  
592 but future work should examine whether  $HS^-$  can also be an important component in the anion  
593 column site as it may behave like  $OH^-$ . Moreover, examination by quantum-mechanical  
594 molecular dynamics (MD) may enable evaluation of the energy and structure of periodic solids  
595 (e.g., minerals) under high pressure or temperature (Segall et al. 2002). Recent studies have  
596 successfully demonstrated applications of ab-initio MD approaches for evaluating hydrothermal  
597 reactions involving molecular or aqueous species (e.g., Sherman 2007; Mei et al. 2013). To our  
598 knowledge, however, the published literature is currently lacking studies applying MD tools to  
599 incorporation into minerals under magmatic-hydrothermal conditions. In this regard, treatment of  
600 high pressure and temperature dynamics (with or without  $H_2O$ ) on S-bearing apatite should be  
601 the subject of future studies.

602 We highlight that the interpretation of S behavior in this study is based on the traditional  
603 paradigm that  $SO_4^{2-}$  and  $S^{2-}$  are the only relevant S species in silicate melts (Baker and  
604 Rutherford, 1996b); however, this assumption has been challenged by the discovery of the S

605 radical ions (e.g.,  $S_2^-$ ,  $S_3^-$ ) in hydrothermal fluids and silicate melts (Winther et al. 1998;  
606 Jacquemet et al. 2014; Pokrovski and Dubessy 2015) and by the possible presence of (un-  
607 quenchable)  $S^{4+}$  in silicate melts (Métrich et al. 2009). Therefore, it is important to consider the  
608 role of various S species and oxidation states in geological fluids and melts when S-bearing  
609 phases (e.g., apatite) that are subject to high temperatures and pressures are investigated in future  
610 studies.

611

612

### IMPLICATIONS

613 This study addresses the structural incorporation of multiple oxidation states of S into apatite  
614 and the response of the apatite structure to these substituents. The crystallographic characteristics  
615 and energetic stability of the S-incorporated apatite structure vary depending on the S oxidation  
616 state and can be significantly influenced by [1] the neighboring column anion ( $F^-$ ,  $Cl^-$ , or  $OH^-$ ), [2]  
617 the concomitant substitutions for  $Ca^{2+}$  and  $P^{5+}$  (e.g.,  $La^{3+}$ ,  $Na^+$ ,  $Si^{4+}$ ) and their site preferences  
618 (particularly between the Ca1 and Ca2 site), and [3] the molecular geometry and orientation of S  
619 oxyanions in the structure.

620 Sulfide ( $S^{2-}$ ) occupancy in the anion column site ( $S^{2-}$  + vacancy) in the apatite structure is a  
621 likely mechanism in reduced geological systems (e.g., around fayalite-magnetite-quartz (FMQ)  
622 buffer). Of the model configurations tested, the scenarios with  $S^{2-}$  accommodated in the  
623 chlorapatite structure and with  $S^{2-}$  positioned closely to  $Cl^-$  site in the anion column are most  
624 energetically plausible. In most natural systems, however,  $F^-$ ,  $Cl^-$ , and  $OH^-$  are the three major  
625 column anions in apatite, while S is a trace element, independent of its oxidation state (< 1 wt%  
626 S; Parat et al. 2011; Konecke et al. 2017). Thus, the presence of  $S^{2-}$  in natural apatite is probably

627 not limited to chloroapatite or Cl-rich apatite. The thermodynamic advantage of  $S^{2-}$  in the Cl site  
628 may play a role in determining the S content in apatite that forms under Cl- and S-rich reduced  
629 environments. This is consistent with the positive correlation between Cl and S contents found  
630 from lunar apatite (Boyce et al. 2014) and the XANES-determined presence of  $S^{2-}$  in apatite  
631 crystallized from a mafic melt under reducing redox conditions (~FMQ, Konecke et al. 2017).

632 The energetics data about  $S^{6+}$  incorporation into the La-bearing apatite support that the  
633 replacement mechanism of  $P^{5+} + Ca^{2+} \leftrightarrow S^{6+} + Na^+$  is energetically more favored over the  
634 mechanism of  $2P^{5+} \leftrightarrow S^{6+} + Si^{4+}$ . However, it seems important to consider all replacement  
635 mechanisms in natural systems where sulfate is only a minor substituent for phosphate in apatite  
636 as documented for apatite from the Yerington batholith (Streck and Dilles 1998). The results for  
637 oxidized sulfur species ( $S^{4+}$ ,  $S^{6+}$ ) presented in this study indicate that there are more energetic or  
638 geometric constraints (e.g., the orientation of the S lone pair electrons) on  $SO_3^{2-}$  incorporation  
639 into the apatite structure than on  $SO_4^{2-}$  incorporation. The data from this study and Konecke et al.  
640 (2017) support the hypothesis that the substitution of  $SO_3^{2-}$  into apatite is relatively minor, but  
641 appreciable if coexisting with  $SO_4^{2-}$  in apatite formed under oxidizing conditions.

642 The abundance and relative proportions of  $S^{2-}$ ,  $S^{4+}$  and  $S^6$  in geologic systems is a function of  
643 oxygen fugacity ( $fO_2$ ), and recorded directly in the S chemistry of apatite (Konecke et al. 2017).  
644 The modeling of different S species in the apatite structure in this study, combined with the  
645 experimental results reported by Konecke et al (2017), implies that the oxidation state of S in  
646 apatite has the potential to serve as a geochemical proxy to probe the  $fO_2$  of magmatic and  
647 hydrothermal systems.

648

649

## ACKNOWLEDGEMENTS

650 Y.K. acknowledges support from Samsung Scholarship. A.F and A.C.S acknowledge the US  
651 National Science Foundation EAR-grant #1524394. B.A.K acknowledges support from Rackham  
652 Graduate School (UM) and a Society of Economic Geologists Student Research Grant. Finally,  
653 we thank J. Rakovan, G. Pokrovski, D. Harlov, and one anonymous reviewer for their  
654 constructive reviews, and are grateful for the editorial handling of F. Nestola.

655

## REFERENCES

- 656 Andersen, L., and Lindqvist, O. (1984) Neutron diffraction refinement of magnesium sulfite  
657 hexahydrate,  $\text{MgSO}_3 \cdot 6\text{H}_2\text{O}$ . Acta Crystallographica Section C: Crystal Structure  
658 Communications, 40, 584-586.
- 659 Baker, L.L., and Rutherford, M.J. (1996a) Crystallisation of anhydrite-bearing magmas.  
660 Geological Society of America Special Papers, 315, 243-250.
- 661 Baker, L.L., and Rutherford, M.J. (1996b) Sulfur diffusion in rhyolite melts. Contributions to  
662 Mineralogy and Petrology, 123, 335-344.
- 663 Boyce, J.W., Tomlinson, S.M., McCubbin, F.M., Greenwood, J.P., and Treiman, A.H. (2014)  
664 The lunar apatite paradox. Science (New York, N.Y.), 344, 400–402.
- 665 Burns, R., and Fyfe, W. (1966) Distribution of elements in geological processes. Chemical  
666 Geology, 1, 49-56.
- 667 Corno, M., Busco, C., Civalleri, B., and Ugliengo, P. (2006) Periodic ab initio study of structural  
668 and vibrational features of hexagonal hydroxyapatite  $\text{Ca}_{10}(\text{PO}_4)_6(\text{OH})_2$ . Physical Chemistry  
669 Chemical Physics, 8, 2464-2472.
- 670 Elliott, B. (2001) Crystallization conditions of the Wiborg rapakivi batholith, SE Finland: an  
671 evaluation of amphibole and biotite mineral chemistry. Mineralogy and Petrology, 72, 305-  
672 324.
- 673 Fiege, A., Holtz, F., Behrens, H., Mandeville, C.W., Shimizu, N., Crede, L.S., and Goettlicher, J.  
674 (2015) Experimental investigation of the S and S-isotope distribution between  $\text{H}_2\text{O}$ -S±Cl  
675 fluids and basaltic melts during decompression. Chemical Geology, 393, 36-54.
- 676 Fleet, M.E., and Pan, Y. (1995) Site preference of rare earth elements in fluorapatite. American  
677 Mineralogist, 80, 329-335.

- 678 Fleet, M.E., and Liu, X. (2007) Coupled substitution of type A and B carbonate in sodium-  
679 bearing apatite. *Biomaterials*, 28, 916-926.
- 680 Foerster, H.-J. (1998) The chemical composition of REE-Y-Th-U-rich accessory minerals in  
681 peraluminous granites of the Erzgebirge-Fichtelgebirge region, Germany, Part I: The  
682 monazite-(Ce)-brabantite solid solution series. *American Mineralogist*, 83, 259-272.
- 683 Greenwood, J.P., Itoh, S., Sakamoto, N., Warren, P., Taylor, L., and Yurimoto, H. (2011)  
684 Hydrogen isotope ratios in lunar rocks indicate delivery of cometary water to the Moon.  
685 *Nature Geoscience*, 4, 79-82.
- 686 Harlov, D.E. (2015) Apatite: a fingerprint for metasomatic processes. *Elements*, 11, 171-176.
- 687 Henning, P., Adolfsson, E., and Grins, J. (2000) The chalcogenide phosphate apatites  
688  $\text{Ca}_{10}(\text{PO}_4)_6\text{S}$ ,  $\text{Sr}_{10}(\text{PO}_4)_6\text{S}$ ,  $\text{Ba}_{10}(\text{PO}_4)_6\text{S}$  and  $\text{Ca}_{10}(\text{PO}_4)_6\text{Se}$ . *Zeitschrift für Kristallographie*  
689 *International journal for structural, physical, and chemical aspects of crystalline materials*,  
690 215, 226.
- 691 Hsu, H., Blaha, P., Cococcioni, M., and Wentzcovitch, R.M. (2011) Spin-state crossover and  
692 hyperfine interactions of ferric iron in  $\text{MgSiO}_3$  perovskite. *Physical Review Letters*, 106,  
693 118501.
- 694 Hughes, J.M., Cameron, M., and Crowley, K.D. (1989) Structural variations in natural F, OH,  
695 and Cl apatites. *American Mineralogist*, 74, 870-876.
- 696 Hughes, J.M., Cameron, M., and Crowley, K.D. (1990) Crystal structures of natural ternary  
697 apatites; solid solution in the  $\text{Ca}_5(\text{PO}_4)_3\text{X}$  (X= F, OH, Cl) system. *American Mineralogist*,  
698 75, 295-304.
- 699 Hughes, J.M., Cameron, M., and Mariano, A.N. (1991) Rare-earth-element ordering and  
700 structural variations in natural rare-earth-bearing apatites. *American Mineralogist*, 76, 1165-  
701 1173.
- 702 Hughes, J.M., and Rakovan, J. (2002) The crystal structure of apatite,  $\text{Ca}_5(\text{PO}_4)_3(\text{F}, \text{OH}, \text{Cl})$ .  
703 *Reviews in mineralogy and geochemistry*, 48, 1-12.
- 704 Hughes, J.M. (2015) Presidential Address. The many facets of apatite. *American Mineralogist*,  
705 100, 1033-1039.
- 706 Hughes, J.M., and Rakovan, J.F. (2015) Structurally robust, chemically diverse: apatite and  
707 apatite supergroup minerals. *Elements*, 11, 165-170.
- 708 Hughes, J.M., Harlov, D., Kelly, S.R., Rakovan, J., and Wilke, M. (2016) Solid solution in the  
709 apatite OH-Cl binary system: Compositional dependence of solid-solution mechanisms in  
710 calcium phosphate apatites along the Cl-OH binary. *American Mineralogist*, 101, 1783-  
711 1791.
- 712 Imai, A. (2002) Metallogenesis of Porphyry Cu Deposits of the Western Luzon Arc, Philippines:  
713 K-Ar ages,  $\text{SO}_3$  Contents of Microphenocrystic Apatite and Significance of Intrusive Rocks.  
714 *Resource Geology*, 52, 147-161.



- 715 Jacquemet, N., Guillaume, D., Zwick, A., and Pokrovski, G.S. (2014) In situ Raman  
716 spectroscopy identification of the  $S_3^-$  ion in S-rich hydrothermal fluids from synthetic fluid  
717 inclusions. *American Mineralogist*, 99, 1109-1118.
- 718 Jugo, P.J., Luth, R.W., and Richards, J.P. (2005) Experimental data on the speciation of sulfur as  
719 a function of oxygen fugacity in basaltic melts. *Geochimica et Cosmochimica Acta*, 69, 497-  
720 503.
- 721 Klein, C., and Dutrow, B. (2002) *Manual of mineral science (manual of mineralogy)*. John Wiley.
- 722 Konecke, B.A., Fiege, A., Simon, A.C., Parat, F., and Stechern, A. (2017) Co-variability of  $S^{6+}$ ,  
723  $S^{4+}$ , and  $S^{2-}$  in apatite as a function of oxidation state: Implications for a new oxybarometer.  
724 *American Mineralogist*, 102, 548-557.
- 725 Lattard, D., and Evans, B.W. (1992) New experiments on the stability of grunerite. *European*  
726 *journal of mineralogy*, 4, 219-238.
- 727 Liu, Y., and Comodi, P. (1993) Some aspects of the crystal-chemistry of apatites. *Mineralogical*  
728 *magazine*, 57, 709-720.
- 729 Mei, Y., Sherman, D.M., Liu, W., and Brugger, J. (2013) Complexation of gold in  $S_3^-$ -rich  
730 hydrothermal fluids: Evidence from ab-initio molecular dynamics simulations. *Chemical*  
731 *geology*, 347, 34-42.
- 732 Métrich, N., Berry, A.J., O'Neill, H.S.C., and Susini, J. (2009) The oxidation state of sulfur in  
733 synthetic and natural glasses determined by X-ray absorption spectroscopy. *Geochimica et*  
734 *Cosmochimica Acta*, 73, 2382-2399.
- 735 Monkhorst, H.J., and Pack, J.D. (1976) Special points for Brillouin-zone integrations. *Physical Review B*, 13, 5188.
- 736 Monkhorst, H.J., and Pack, J.D. (1976) Special points for Brillouin-zone integrations. *Physical*  
737 *review B*, 13, 5188.
- 738 Pan, Y., and Fleet, M.E. (2002) Compositions of the apatite-group minerals: substitution  
739 mechanisms and controlling factors. *Reviews in Mineralogy and Geochemistry*, 48, 13-49.
- 740 Parat, F., Dungan, M.A., and Streck, M.J. (2002) Anhydrite, pyrrhotite, and sulfur-rich apatite:  
741 tracing the sulfur evolution of an Oligocene andesite (Eagle Mountain, CO, USA). *Lithos*,  
742 64, 63-75.
- 743 Parat, F., and Holtz, F. (2004) Sulfur partitioning between apatite and melt and effect of sulfur  
744 on apatite solubility at oxidizing conditions. *Contributions to Mineralogy and Petrology*,  
745 147, 201-212.
- 746 Parat, F., and Holtz, F. (2005) Sulfur partition coefficient between apatite and rhyolite: the role  
747 of bulk S content. *Contributions to Mineralogy and Petrology*, 150, 643-651.
- 748 Parat, F., Holtz, F., and Streck, M.J. (2011) Sulfur-bearing magmatic accessory minerals.  
749 *Reviews in Mineralogy and Geochemistry*, 73, 285-314.
- 750 Paris, E., Giuli, G., Carroll, M.R., and Davoli, I. (2001) The valence and speciation of sulfur in  
751 glasses by X-ray absorption spectroscopy. *The Canadian Mineralogist*, 39, 331-339.

- 752 Pearson, R.G. (1968) Hard and soft acids and bases, HSAB, part 1: Fundamental principles.  
753 Journal of Chemical Education, 45, 581.
- 754 Peng, G., Luhr, J.F., and McGee, J.J. (1997) Factors controlling sulfur concentrations in volcanic  
755 apatite. American Mineralogist, 82, 1210-1224.
- 756 Perdew, J.P., Burke, K., and Ernzerhof, M. (1996) Generalized gradient approximation made  
757 simple. Physical review letters, 77, 3865.
- 758 Pokrovski, G.S., and Dubessy, J. (2015) Stability and abundance of the trisulfur radical ion in  
759 hydrothermal fluids. Earth and Planetary Science Letters, 411, 298-309.
- 760 Rakovan, J.F., and Hughes, J.M. (2000) Strontium in the apatite structure: strontian fluorapatite  
761 and belovite-(Ce). The Canadian Mineralogist, 38, 839-845.
- 762 Rakovan, J., and Waychunas, G. (2013) Apatite—The Great Pretender. Mineral Monographs 17.
- 763 Rohrbach, A., Hafner, J., and Kresse, G. (2003) Electronic correlation effects in transition-metal  
764 sulfides. Journal of Physics: Condensed Matter, 15, 979.
- 765 Rouse, R.C., and Dunn, P.J. (1982) A contribution to the crystal chemistry of ellestadite and the  
766 silicate sulfate apatites. American Mineralogist, 67, 90-96.
- 767 Rulis, P., Ouyang, L., and Ching, W. (2004) Electronic structure and bonding in calcium apatite  
768 crystals: Hydroxyapatite, fluorapatite, chlorapatite, and bromapatite. Physical Review B, 70,  
769 155104.
- 770 Sato, M., Hickling, N., and McLane, J.E. (1973) Oxygen fugacity values of Apollo 12, 14, and  
771 15 lunar samples and reduced state of lunar magmas, Lunar and Planetary Science  
772 Conference Proceedings, p. 1061.
- 773 Segall, M., Lindan, P.J., Probert, M.a., Pickard, C., Hasnip, P., Clark, S., and Payne, M. (2002)  
774 First-principles simulation: ideas, illustrations and the CASTEP code. Journal of Physics:  
775 Condensed Matter, 14, 2717.
- 776 Shannon, R.t. (1976) Revised effective ionic radii and systematic studies of interatomic distances  
777 in halides and chalcogenides. Acta Crystallographica Section A: Crystal Physics, Diffraction,  
778 Theoretical and General Crystallography, 32, 751-767.
- 779 Sherman, D.M. (2007) Complexation of Cu<sup>+</sup> in hydrothermal NaCl brines: ab initio molecular  
780 dynamics and energetics. Geochimica et Cosmochimica Acta, 71, 714-722.
- 781 Shuller, L.C., Ewing, R.C., and Becker, U. (2013) Np-incorporation into uranyl phases: A  
782 quantum-mechanical evaluation. Journal of Nuclear Materials, 434, 440-450.
- 783 Shuller, L.C., Bender, W.M., Walker, S.M., and Becker, U. (2014) Quantum-mechanical  
784 methods for quantifying incorporation of contaminants in proximal minerals. Minerals, 4,  
785 690-715.
- 786 Smith, F.N., Um, W., Taylor, C.D., Kim, D.-S., Schweiger, M.J., and Kruger, A.A. (2016)  
787 Computational Investigation of Technetium (IV) Incorporation into Inverse Spinels:

- 788 Magnetite ( $\text{Fe}_3\text{O}_4$ ) and Trevorite ( $\text{NiFe}_2\text{O}_4$ ). *Environmental Science & Technology*, 50,  
789 5216-5224.
- 790 Stackhouse, S., Stixrude, L., and Karki, B.B. (2010) Determination of the high-pressure  
791 properties of fayalite from first-principles calculations. *Earth and Planetary Science Letters*,  
792 289, 449-456.
- 793 Streck, M.J., and Dilles, J.H. (1998) Sulfur evolution of oxidized arc magmas as recorded in  
794 apatite from a porphyry copper batholith. *Geology*, 26, 523-526.
- 795 Tepper, J.H., and Kuehner, S.M. (1999) Complex zoning in apatite from the Idaho batholith: A  
796 record of magma mixing and intracrystalline trace element diffusion. *American*  
797 *Mineralogist*, 84, 581-595.
- 798 Ulian, G., Valdrè, G., Corno, M., and Ugliengo, P. (2013) Periodic ab initio bulk investigation of  
799 hydroxylapatite and type A carbonated apatite with both pseudopotential and all-electron  
800 basis sets for calcium atoms. *American Mineralogist*, 98, 410-416.
- 801 Walker, S.M., and Becker, U. (2015) Uranyl (VI) and neptunyl (V) incorporation in carbonate  
802 and sulfate minerals: Insight from first-principles. *Geochimica et Cosmochimica Acta*, 161,  
803 19-35.
- 804 Winther, K.T., Watson, E.B., and Korenowski, G.M. (1998) Magmatic sulfur compounds and  
805 sulfur diffusion in albite melt at 1 GPa and 1300–1500 C. *American Mineralogist*, 83, 1141-  
806 1151.

807

808

809

## FIGURE CAPTIONS

810 **Figure 1.** S XANES analysis of apatite crystallized from a mafic melt at 1,000 °C, 300 MPa and  
811 different  $f\text{O}_2$  conditions (modified from Figure 2 in Konecke et al. (2017)).

812 **Figure 2. (a)** The column anion site and the nearest Ca (Ca2) and P atoms in the hexagonal  
813 apatite structure viewed parallel to the c-axis. **(b)** The coordination environment of X (= F, OH,  
814 Cl) on the plane of  $z = 3/4$  in the host or  $\text{S}^{6+}$ -incorporated apatite where A1 = P or Si, A2 = P or  
815 S, C1 = Ca or Na and C2 = Ca or La. Atoms Ca, C1 and C2 form the triangle whose corners are  
816 Ca2 sites. In both **(a)** and **(b)**, oxygen atoms are omitted.

817 **Figure 3.** Examples of S-incorporated apatite models. (a) The unit cell of  $\text{SO}_4^{2-}$ - and  $\text{SO}_3^{2-}$ -  
818 incorporated fluorapatite,  $\text{Ca}_9\text{Na}(\text{PO}_4)_3(\text{SiO}_4)(\text{SO}_4)(\text{SO}_3)\text{F}_2$  and (b) the  $1\times 1\times 2$  supercell of  $\text{S}^{2-}$ -  
819 incorporated apatite,  $\text{Ca}_{20}(\text{PO}_4)_{12}\text{SF}_2$ .

820 **Figure 4.** Atomistic-level view of (a)  $\text{SO}_4^{2-}$  near the F column in  $\text{S}^{6+}$ -incorporated Na-bearing  
821 apatite and (b) A-type and (c) B-type  $\text{SO}_3^{2-}$  near the F column in  $\text{S}^{6+}$  and  $\text{S}^{4+}$  co-incorporated  
822 apatite. Orbital contours for  $\text{SO}_3^{2-}$  are shown to indicate the lone pair (l.p.) electrons and S-O  
823 bonding (see text for more details).

824 **Figure 5.** The optimized positions of column anions in hexagonal end-member and partially  $\text{S}^{2-}$ -  
825 incorporated apatite in the  $1\times 1\times 2$  supercell. (a) fluorapatite (b) chlorapatite and (c)  
826 hydroxylapatite systems are depicted respectively. Initial  $\text{S}^{2-}$  is referred to as  $\text{S}(\text{F}, \text{Cl}, \text{OH})_{\text{ini}}$  to  
827 denote a position near the anion column chosen as the initial  $\text{S}^{2-}$  position replacing  $\text{F}^-$ ,  $\text{Cl}^-$  and  
828  $\text{OH}^-$ . The fractional coordinate of z (with respect to the unit cell) in the optimized structure is  
829 presented for S at or near  $z = 3/4$ . Note that the column anion site at  $z = 7/4$  (coordinate with  
830 respect to the original  $1\times 1\times 1$  unit cell, not shown) is vacant in the supercell whose zero charge is  
831 compensated with a charge of 2- from S.

832

833

834

## TABLES

835

836 **Table 1.** Lattice parameters for natural and calculated (CASTEP) apatite

	$a$ (Å)	$c$ (Å)	$z$ value <sup>b</sup> of (F, Cl, OH)
<u>Fluorapatite</u>			
Calculated	9.469	6.894	0.2500
Natural <sup>a</sup>	9.397	6.878	0.2500
Deviation (%)	0.76	0.22	
<u>Chlorapatite</u>			
Calculated	9.525	6.895	0.0621
Natural <sup>a</sup>	9.598	6.776	0.0677
Deviation (%)	0.76	1.76	
<u>Hydroxylapatite</u>			
Calculated	9.763	6.757	0.2128
Natural <sup>a</sup>	9.417	6.875	0.1979
Deviation (%)	3.68	1.71	

837

838 *Notes:* <sup>a</sup> Hughes and Rakovan (2002) <sup>b</sup> The  $z$  value of anion column position (0, 0,  $z$ ).

839

840 **Table 2.** Reaction equations and energies of incorporation of  $S^{6+}$  and co-incorporation of  $S^{4+}$   
 841 with  $S^{6+}$  into apatite.

Incorporation reaction	$\Delta E_{rxn}$ (kJ/mol)		
	X = F	Cl	OH
<hr/>			
$S^{6+}$ -incorporation into La-bearing apatite	X = F	Cl	OH
Na-bearing: $[Ca_8NaLa][(PO_4)_6]X_2 + CaSO_4 \leftrightarrow [Ca_9Na][(PO_4)_5(SO_4)]X_2 + LaPO_4$	-1.74	1.16	4.34
Si-bearing: $[Ca_9La][(PO_4)_5(SiO_4)]X_2 + CaSO_4 \leftrightarrow [Ca_{10}][(PO_4)_4(SiO_4)(SO_4)]X_2 + LaPO_4$	15.44	5.02	15.44
<hr/>			
$S^{4+}, S^{6+}$ -incorporation into La-bearing apatite	X = F	Cl	OH
$[Ca_7La_2Na][(PO_4)_5(SiO_4)](F, Cl, OH)_2 + 2CaSO_4 + Ni \leftrightarrow [Ca_9Na][(PO_4)_3(SiO_4)(SO_4)(SO_3)](F, Cl, OH)_2 + 2LaPO_4 + NiO$			
A-type $S^{4+}$	117.71	95.52	117.71
B-type $S^{4+}$	132.19	111.92	131.22
<hr/>			

842

843

844 **Table 3.** Summary of geometric parameters for  $\text{SO}_4^{2-}$  incorporated apatite phases.

Optimized structure	Cell volume ( $\text{\AA}^3$ )	X-S distance <sup>a</sup> ( $\text{\AA}$ )	O-S-O angle <sup>a</sup> (degree)
<b>Fluorapatite</b>			
S, Na-bearing	538.9	3.68	107.9
S, Si-bearing	541.1	3.55	107.6
End-member	535.3	3.64	107.2
<b>Chorapatite</b>			
S, Na-bearing	563.7	4.02	108.3
S, Si-bearing	568.4	3.92	108.2
End-member	560.6	3.97	107.7
<b>Hydroxylapatite</b>			
S, Na-bearing	545.9	3.73	108.2
S, Si-bearing	547.6	3.61	108.4
End-member	541.8	3.67	107.6

845

846 *Notes:* <sup>a</sup> For the apatite end-members, ( $\text{F}^-$ ,  $\text{Cl}^-$ , or  $\text{OH}^-$ )-S distance and O-S-O angle is measured  
847 for P in place of S.

848

849 **Table 4.** Summary of geometric parameters for  $\text{SO}_4^{2-}$  and  $\text{SO}_3^{2-}$  incorporated apatite.

Optimized structure	Cell volume ( $\text{\AA}^3$ )	X-S <sup>4+</sup> distance ( $\text{\AA}$ )	X-S <sup>6+</sup> distance ( $\text{\AA}$ )	z <sup>a</sup> of S <sup>4+</sup>	z <sup>a</sup> of S <sup>6+</sup>
<b>Fluorapatite</b>					
Incorporation of					
A-type $\text{SO}_3^{2-}$	542.3	3.63	3.61	0.2230	0.7507
B-type $\text{SO}_3^{2-}$	543.9	3.68	3.68	0.2500	0.7500
<b>Chlorapatite</b>					
A-type $\text{SO}_3^{2-}$	570.4	3.75	3.85	0.2204	0.7502
B-type $\text{SO}_3^{2-}$	574.5	3.97	3.94	0.2462	0.7503
<b>Hydroxylapatite</b>					
A-type $\text{SO}_3^{2-}$	548.5	3.67	3.64	0.2186	0.7461
B-type $\text{SO}_3^{2-}$	551.7	3.73	3.74	0.2432	0.7533

850 *Notes:* <sup>a</sup> The z value of fractional coordination (x, y, z)

851



852 **Table 5.** Reaction equations and energies of S<sup>2-</sup> full and partial incorporation into apatite.

	$\Delta E_{rxn}$ (kJ/mol)		
	Column geometry of S <sup>2-</sup>		
Fe-S system	S(F) <sub>ini</sub>	S(Cl) <sub>ini</sub>	S(OH) <sub>ini</sub>
<u>Full incorporation</u>			
$\text{Ca}_{10}(\text{PO}_4)_6\text{F}_2 + \text{FeS} \leftrightarrow \text{Ca}_{10}(\text{PO}_4)_6(\text{S}) + \text{FeF}_2$	362.02 (232.83) <sup>a)</sup>	–	–
$\text{Ca}_{10}(\text{PO}_4)_6\text{Cl}_2 + \text{FeS} \leftrightarrow \text{Ca}_{10}(\text{PO}_4)_6(\text{S}) + \text{FeCl}_2$	–	105.11	–
<u>Partial incorporation</u>			
$\text{Ca}_{20}(\text{PO}_4)_{12}\text{F}_4 + \text{FeS} \leftrightarrow \text{Ca}_{20}(\text{PO}_4)_{12}(\text{S})\text{F}_2 + \text{FeF}_2$	399.53	343.37	344.21
$\text{Ca}_{20}(\text{PO}_4)_{12}\text{Cl}_4 + \text{FeS} \leftrightarrow \text{Ca}_{20}(\text{PO}_4)_{12}(\text{S})\text{Cl}_2 + \text{FeCl}_2$	101.77	97.10	102.83
<u>Na-S system</u>			
<u>Full incorporation</u>			
$\text{Ca}_{10}(\text{PO}_4)_6\text{F}_2 + \text{Na}_2\text{S} \leftrightarrow \text{Ca}_{10}(\text{PO}_4)_6(\text{S}) + 2\text{NaF}_2$	203.76 (74.59) <sup>a)</sup>	–	–
$\text{Ca}_{10}(\text{PO}_4)_6\text{Cl}_2 + \text{Na}_2\text{S} \leftrightarrow \text{Ca}_{10}(\text{PO}_4)_6(\text{S}) + 2\text{NaCl}$	–	-61.32	–
<u>Partial incorporation</u>			
$\text{Ca}_{20}(\text{PO}_4)_{12}\text{F}_4 + \text{Na}_2\text{S} \leftrightarrow \text{Ca}_{20}(\text{PO}_4)_{12}(\text{S})\text{F}_2 + 2\text{NaF}_2$	241.27	185.11	185.95
$\text{Ca}_{20}(\text{PO}_4)_{12}\text{Cl}_4 + \text{Na}_2\text{S} \leftrightarrow \text{Ca}_{20}(\text{PO}_4)_{12}(\text{S})\text{Cl}_2 + 2\text{NaCl}$	-64.66	-69.33	-63.60
<u>Fe-Si-S system</u>			
<u>Full incorporation</u>			
$\text{Ca}_{10}(\text{PO}_4)_6(\text{OH})_2 + \text{FeS} + 6\text{FeSiO}_3 + 2\text{SiO}_2 \leftrightarrow$ $\text{Ca}_{10}(\text{PO}_4)_6(\text{S}) + \text{Fe}_7\text{Si}_8\text{O}_{22}(\text{OH})_2$			-71.86
<u>Partial incorporation</u>			
$\text{Ca}_{20}(\text{PO}_4)_{12}(\text{OH})_4 + \text{FeS} + 6\text{FeSiO}_3 + 2\text{SiO}_2 \leftrightarrow$ $\text{Ca}_{20}(\text{PO}_4)_{12}(\text{S})(\text{OH})_2 + \text{Fe}_7\text{Si}_8\text{O}_{22}(\text{OH})_2$	58.35	40.97	46.84

853

854 *Notes:* <sup>a</sup> The calculated incorporation energy of S<sup>2-</sup> into fluorapatite when initially positioned at  
 855 (0, 0, 0.7).

856

857

858

859 **Table 6.** The cell and lattice parameters of initial and optimized configurations of S<sup>2-</sup> fully and  
 860 partially incorporated apatite.

Optimized structure	z <sup>b</sup> of (F, Cl, OH) <sub>ini</sub>	Full incorporation		Partial incorporation	
		a (Å)	b (Å)	z <sup>c</sup> of S <sup>2-</sup>	z <sup>c</sup> of S <sup>2-</sup>
S-apatite (experiment) <sup>a</sup>		9.462	6.834	0.5	
S in the fluorapatite structure	0.25 and 0.75	9.825	6.739	0.7500 (0.5016) <sup>d</sup>	0.57
Deviation (%)		3.84	1.39		
S in the chlorapatite structure	0.062 and 0.562	9.566	6.843	0.5018	0.51
Deviation (%)		1.10	0.13		
S in the hydroxyapatite structure	0.213 and 0.713	9.542	6.859	0.5004	0.61
Deviation (%)		0.85	0.36		

861

862 Notes: <sup>a</sup> Henning *et al.* (2000)

863 <sup>b</sup> The z value of column anion position (0, 0, z) used in the initial S<sup>2-</sup> incorporation  
 864 models. In the models, (F, Cl, OH) at or near the mirror plane at z = 3/4 is replaced by S<sup>2-</sup>.

865 <sup>c</sup> The z value of S<sup>2-</sup> position (0, 0, z) in the lowest-energy configurations. See Figure 5 for  
 866 details.

867 <sup>d</sup> The optimized position of S<sup>2-</sup> in fluorapatite when initially positioned at (0, 0, 0.7).

868

869 **Table 7.** Reaction equations and energies of La<sup>3+</sup> - and S<sup>6+</sup> -incorporation into end-member apatite.

La <sup>3+</sup> -incorporation into end-member apatite	$\Delta E_{rxn}$ (kJ/mol)		
	X = F	Cl	OH
La <sup>3+</sup> and Na <sup>+</sup> : Ca <sub>10</sub> (PO <sub>4</sub> ) <sub>6</sub> X <sub>2</sub> + 1/3Na <sub>3</sub> PO <sub>4</sub> + LaPO <sub>4</sub> ↔ [Ca <sub>8</sub> NaLa][(PO <sub>4</sub> ) <sub>6</sub> ]X <sub>2</sub> + 2/3Ca <sub>3</sub> (PO <sub>4</sub> ) <sub>2</sub>	91.28	68.12	77.29
La <sup>3+</sup> and Si <sup>4+</sup> : Ca <sub>10</sub> (PO <sub>4</sub> ) <sub>6</sub> X <sub>2</sub> + Ca <sub>2</sub> SiO <sub>4</sub> + LaPO <sub>4</sub> ↔ [Ca <sub>9</sub> La][(PO <sub>4</sub> ) <sub>5</sub> (SiO <sub>4</sub> )]X <sub>2</sub> + Ca <sub>3</sub> (PO <sub>4</sub> ) <sub>2</sub>	75.45	69.76	70.72
S <sup>6+</sup> -incorporation into end-member apatite	X = F	Cl	OH
S <sup>6+</sup> and Na <sup>+</sup> : Ca <sub>10</sub> (PO <sub>4</sub> ) <sub>6</sub> X <sub>2</sub> + 1/3Na <sub>3</sub> PO <sub>4</sub> + CaSO <sub>4</sub> ↔ [Ca <sub>9</sub> Na][(PO <sub>4</sub> ) <sub>5</sub> (SO <sub>4</sub> )]X <sub>2</sub> + 2/3Ca <sub>3</sub> (PO <sub>4</sub> ) <sub>2</sub>	89.54	69.28	81.63
S <sup>6+</sup> and Si <sup>4+</sup> : Ca <sub>10</sub> (PO <sub>4</sub> ) <sub>6</sub> X <sub>2</sub> + Ca <sub>2</sub> SiO <sub>4</sub> + CaSO <sub>4</sub> ↔ [Ca <sub>10</sub> ][(PO <sub>4</sub> ) <sub>4</sub> (SiO <sub>4</sub> )(SO <sub>4</sub> )]X <sub>2</sub> + Ca <sub>3</sub> (PO <sub>4</sub> ) <sub>2</sub>	90.89	74.78	86.16

870

871

872

873

874

875

876

877

878

879

880

881

882

883

884

885

886

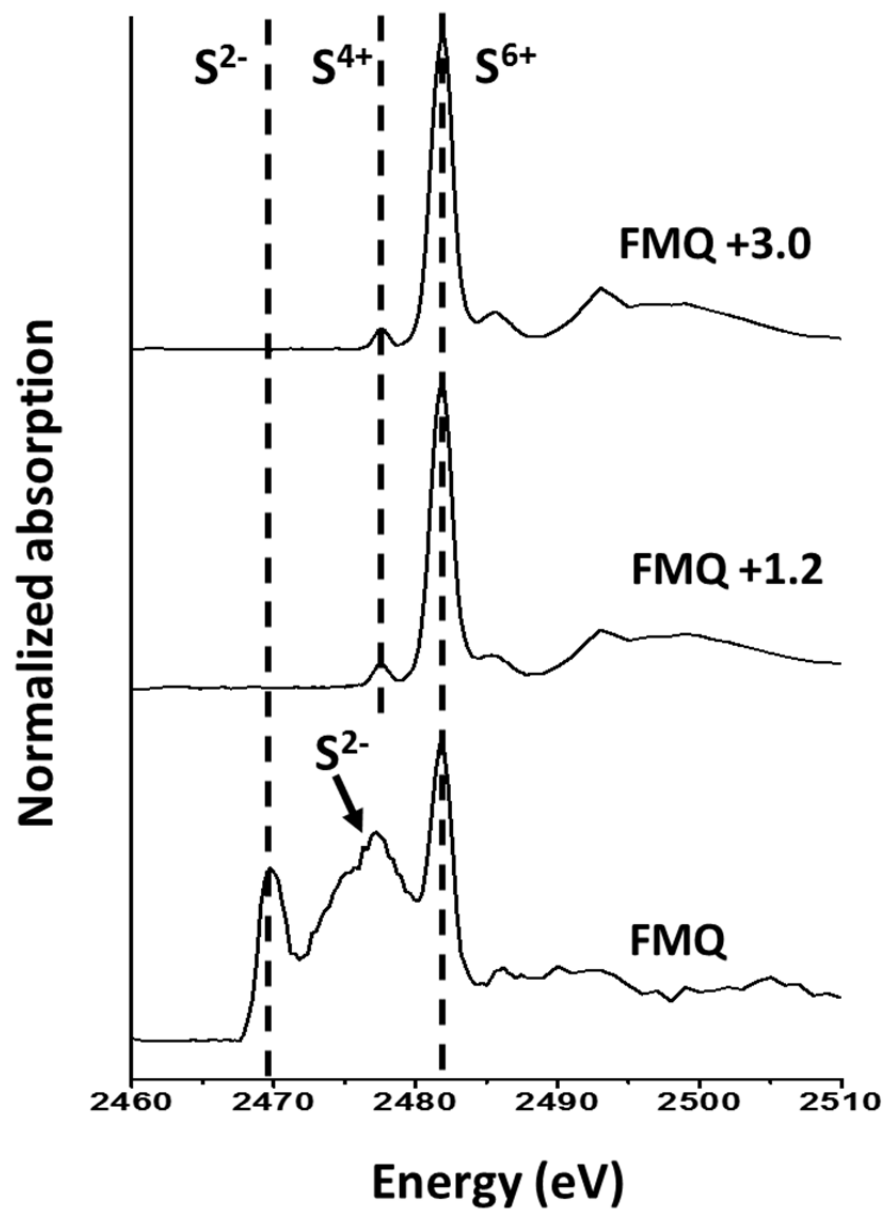
887

888 **Table 8.** Reaction equations and energies of incorporation of  $S^{6+}$  into La- and Na-bearing apatite  
 889 ( $Na^+$  positioned at the Ca1 site and  $La^{3+}$  at the Ca2 site) and of  $Na^+$  exchange between the Ca2  
 890 and Ca1 site of  $S^{6+}$  incorporated apatite.

891

<u>Reaction</u>	$\Delta E_{rxn}$ (kJ/mol)	
$S^{6+}$ -incorporation into La-bearing apatite with $Na^+$ at the Ca1 site	X = F	Cl
Na-bearing: $[Ca_8NaLa][(PO_4)_6]X_2 + CaSO_4 \leftrightarrow$ $[Ca_9Na][(PO_4)_5(SO_4)]X_2 + LaPO_4$	-3.85	-7.85
Exchange of $Na^+$ in the $S^{6+}$ -bearing apatite structure	X = F	Cl
$[Ca_9Na][(PO_4)_5(SO_4)]X_2$ ( $Na^+$ at the Ca2 site) $\leftrightarrow [Ca_9Na][(PO_4)_5(SO_4)]X_2$ ( $Na^+$ at the Ca1 site)	-22.46	-7.76

892

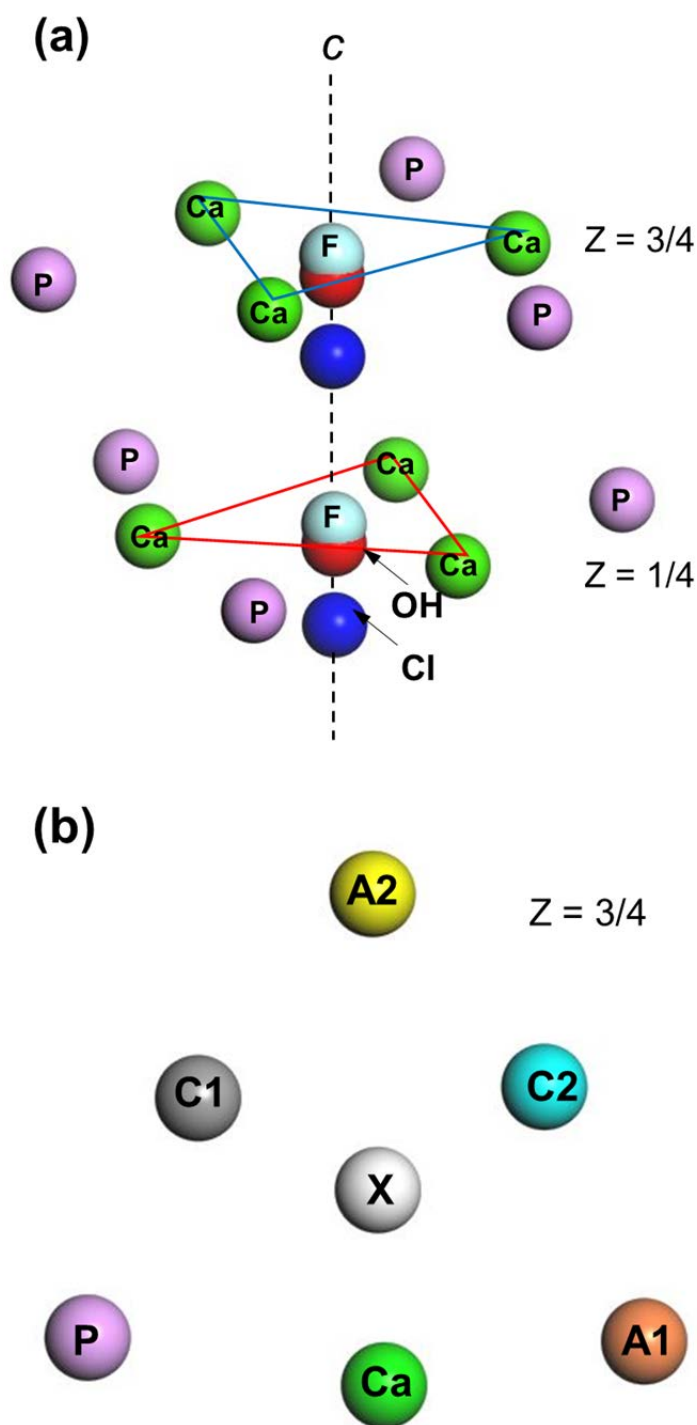


893

894 **Figure 1.** S XANES analysis of apatite crystallized from a mafic melt at 1,000 °C, 300 MPa and  
895 different  $fO_2$  conditions (modified from Figure 2 in Konecke et al. (2017)).

896

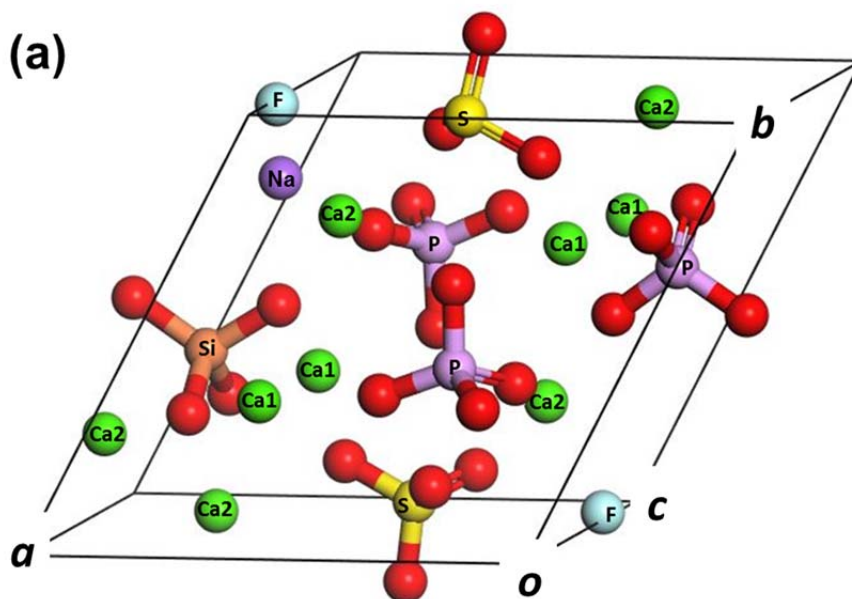
897



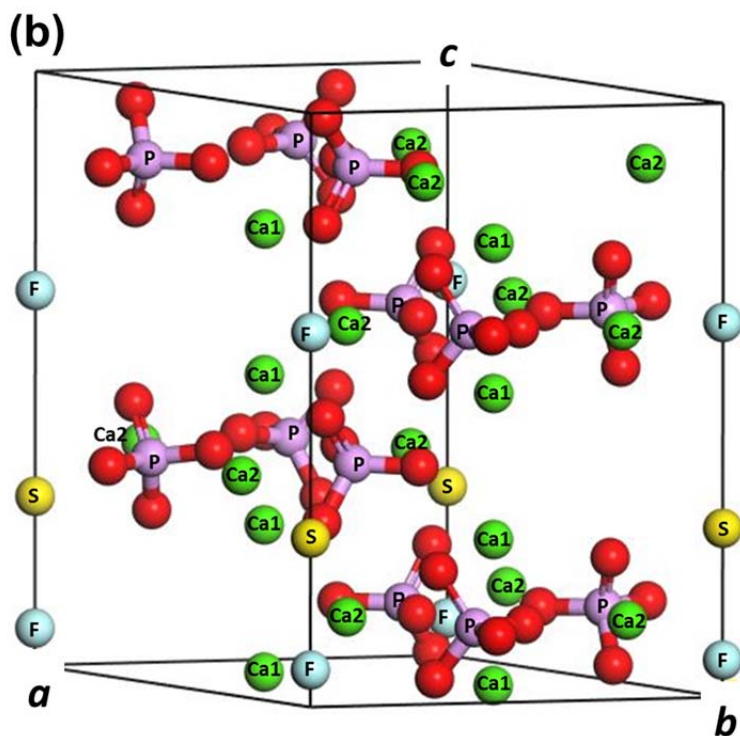
898

899

900 **Figure 2.** (a) The column anion site and the nearest Ca (Ca2) and P atoms in the hexagonal  
 901 apatite structure viewed parallel to the c-axis. (b) The coordination environment of X (= F, OH,  
 902 Cl) on the plane of  $z = 3/4$  in the host or  $S^{6+}$ -incorporated apatite where A1 = P or Si, A2 = P or  
 903 S, C1 = Ca or Na and C2 = Ca or La. Atoms Ca, C1 and C2 form the triangle whose corners are  
 904 Ca2 sites. In both (a) and (b), oxygen atoms are omitted.

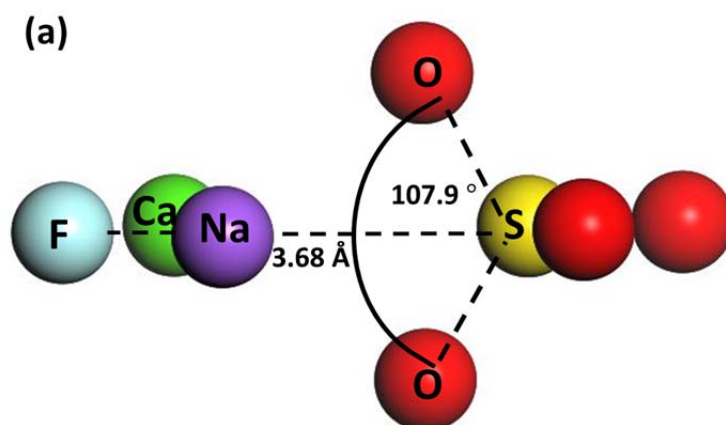


905



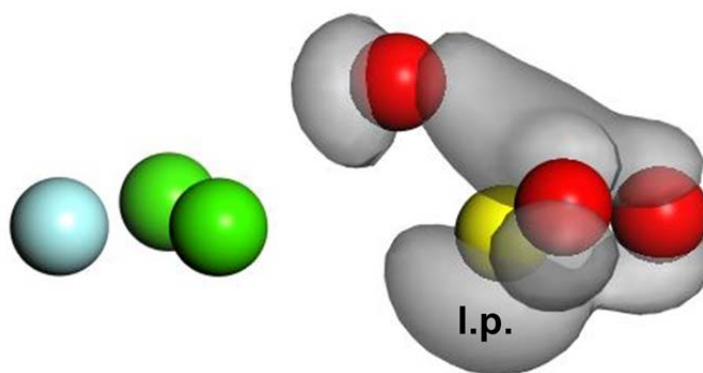
906

907 **Figure 3.** Examples of S-incorporated apatite models. (a) The unit cell of SO<sub>4</sub><sup>2-</sup>- and SO<sub>3</sub><sup>2-</sup>-  
908 incorporated fluorapatite, Ca<sub>9</sub>Na(PO<sub>4</sub>)<sub>3</sub>(SiO<sub>4</sub>)(SO<sub>4</sub>)(SO<sub>3</sub>)F<sub>2</sub> and (b) the 1×1×2 supercell of S<sup>2-</sup>-  
909 incorporated apatite, Ca<sub>20</sub>(PO<sub>4</sub>)<sub>12</sub>SF<sub>2</sub>.



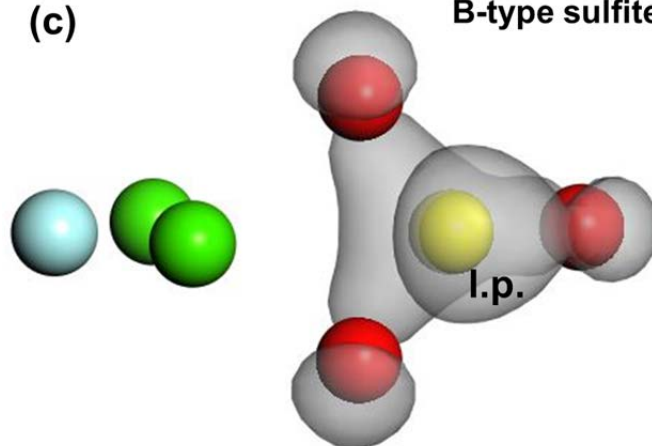
910

(b) A-type sulfite



911

(c) B-type sulfite

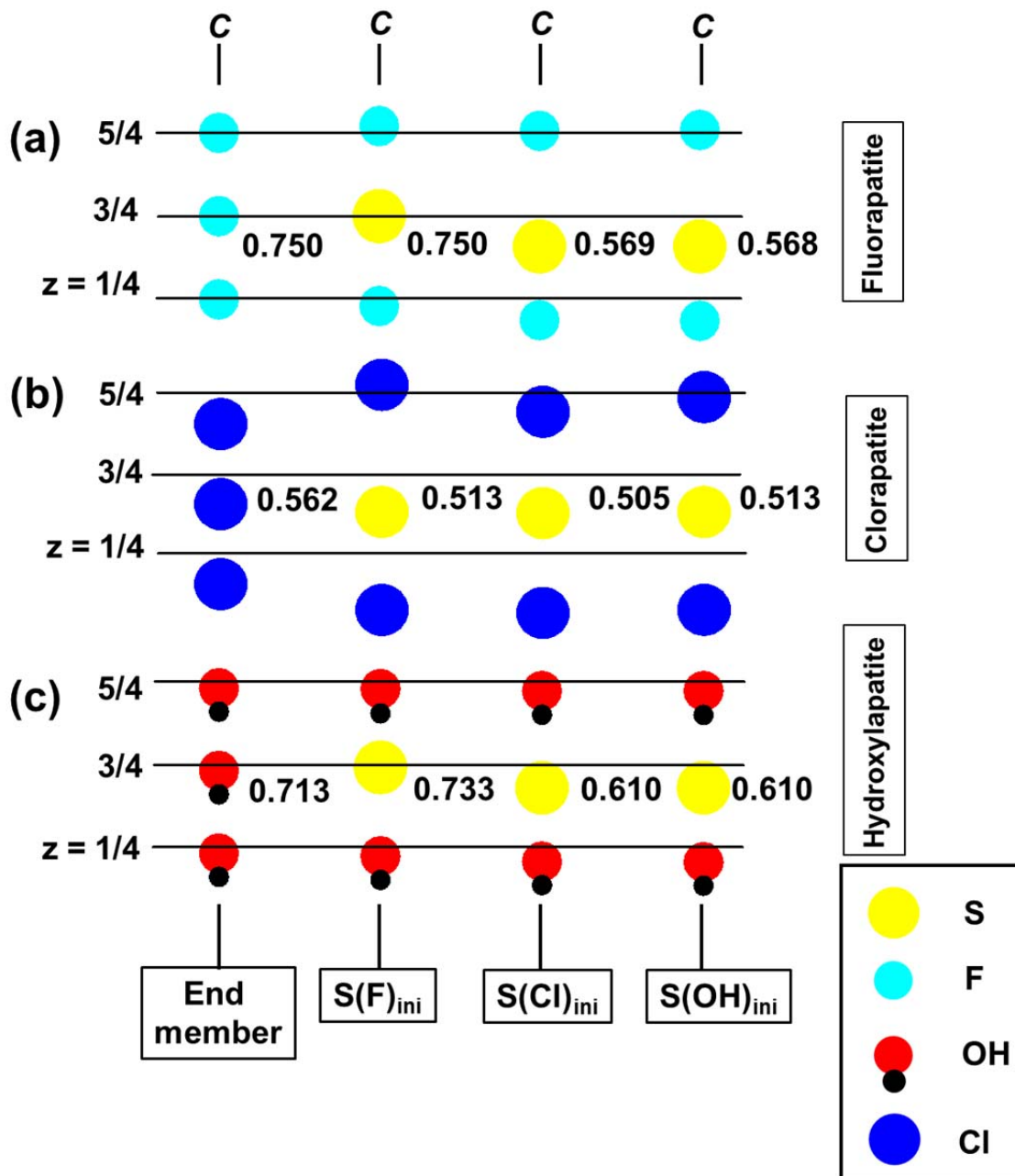


912

913 **Figure 4.** Atomistic-level view of (a)  $\text{SO}_4^{2-}$  near the F column in  $\text{S}^{6+}$ -incorporated Na-bearing  
914 apatite and (b) A-type and (c) B-type  $\text{SO}_3^{2-}$  near the F column in  $\text{S}^{6+}$  and  $\text{S}^{4+}$  co-incorporated  
915 apatite. Orbital contours for  $\text{SO}_3^{2-}$  are shown to indicate the lone pair (l.p.) electrons and S-O  
916 bonding (see text for more details).



917



918

919 **Figure 5.** The optimized positions of column anions in hexagonal end-member and partially  $S^{2-}$ -  
 920 incorporated apatite in the  $1 \times 1 \times 2$  supercell. (a) fluorapatite (b) chlorapatite and (c)  
 921 hydroxylapatite systems are depicted respectively. Initial  $S^{2-}$  is referred to as S (F, Cl, OH)<sub>ini</sub> to  
 922 denote a position near the anion column chosen as the initial  $S^{2-}$  position replacing  $F^-$ ,  $Cl^-$  and  
 923  $OH^-$ . The fractional coordinate of z (with respect to the unit cell) in the optimized structure is  
 924 presented for S at or near  $z = 3/4$ . Note that the column anion site at  $z = 7/4$  (coordinate with

925 respect to the original  $1\times 1\times 1$  unit cell, not shown) is vacant in the supercell whose zero charge is  
926 compensated with a charge of  $2^-$  from S.

927